

# 1 **Rapid O<sub>3</sub> assimilations – Part 2: tropospheric O<sub>3</sub> changes accompanied by** 2 **declines in NO<sub>x</sub> emissions in the US and Europe in 2005-2020**

3  
4 Rui Zhu<sup>1</sup>, Zhaojun Tang<sup>1</sup>, Xiaokang Chen<sup>1</sup>, Xiong Liu<sup>2</sup> and Zhe Jiang<sup>1\*</sup>  
5

6 <sup>1</sup>School of Earth and Space Sciences, University of Science and Technology of China, Hefei,  
7 Anhui, 230026, China.

8 <sup>2</sup>Center for Astrophysics | Harvard & Smithsonian, Cambridge, MA 02138, USA.  
9

10 \*Correspondence to: Zhe Jiang ([zhejiang@ustc.edu.cn](mailto:zhejiang@ustc.edu.cn))  
11  
12

## 13 **Abstract**

14 Tropospheric nitrogen dioxide (NO<sub>2</sub>) concentrations have declined dramatically over the  
15 United States (US) and Europe in recent decades. Here we investigate the changes in surface  
16 and free tropospheric O<sub>3</sub> accompanied by NO<sub>2</sub> changes over the US and Europe in 2005-2020  
17 by assimilating the Ozone Monitoring Instrument (OMI), and US Air Quality System (AQS)  
18 and European AirBase network O<sub>3</sub> observations. The assimilated O<sub>3</sub> concentrations  
19 demonstrate good agreement with O<sub>3</sub> observations: surface O<sub>3</sub> concentrations are 41.4, 39.5  
20 and 39.5 ppb (US) and 35.3, 32.0 and 31.6 ppb (Europe); and tropospheric O<sub>3</sub> columns are 35.5,  
21 37.0 and 36.8 DU (US) and 32.8, 35.3 and 36.4 DU (Europe) in the simulations, assimilations  
22 and observations, respectively. We find overestimated summertime surface O<sub>3</sub> concentrations  
23 over the US and Europe, which resulted in a surface O<sub>3</sub> maximum in July-August in simulations  
24 in contrast to April in observations. Furthermore, our analysis exhibits limited changes in  
25 surface O<sub>3</sub> concentrations, i.e., decreased by -6% over the US and increased by 1.5% over  
26 Europe in 2005-2020. The surface observation-based assimilations suggest insignificant  
27 changes in tropospheric O<sub>3</sub> columns: -3.0% (US) and 1.5% (Europe) in 2005-2020. While the  
28 OMI-based assimilations exhibit larger decreases in tropospheric O<sub>3</sub> columns, -12.0% (US)  
29 and -15.0% (Europe) in 2005-2020, the decreases mainly occurred in 2010-2014,  
30 corresponding to the reported slowed declines in free tropospheric NO<sub>2</sub> since 2010. Our  
31 analysis thus suggests limited impacts of local emission declines on tropospheric O<sub>3</sub> over the

32 US and Europe and advises more efforts to evaluate the possible contributions of natural  
33 sources and transport. The discrepancy in assimilated tropospheric O<sub>3</sub> columns further  
34 indicates the possible uncertainties in the derived tropospheric O<sub>3</sub> changes.

35

## 36 **1. Introduction**

37 The successful emission regulations employed in the United States (US) and Europe  
38 (Crippa et al., 2016; EPA, 2017) have led to dramatic decreases in anthropogenic NO<sub>x</sub>  
39 emissions (Di et al., 2020; Macdonald et al., 2021; Jiang et al., 2022). As an important air  
40 pollutant, tropospheric ozone (O<sub>3</sub>) is produced when volatile organic compounds (VOCs) are  
41 photochemically oxidized in the presence of nitrogen oxides (NO<sub>x</sub>). As a major precursor of  
42 tropospheric O<sub>3</sub>, decreases in surface nitrogen dioxide (NO<sub>2</sub>) concentrations, driven by declines  
43 in NO<sub>x</sub> emissions, have led to marked decreases in surface O<sub>3</sub> concentrations over the US and  
44 Europe in recent decades. For example, Chen et al. (2021) found a decrease in surface O<sub>3</sub>  
45 concentrations from approximately 60 to 45 ppb over the US in 1990-2019; Seltzer et al. (2020)  
46 exhibited a decreasing trend of surface O<sub>3</sub> by approximately 0.8 ppb yr<sup>-1</sup> over the US in 2000-  
47 2015; and Yan et al. (2018) found a decreasing trend of surface O<sub>3</sub> concentrations by  
48 approximately 0.32 μg/m<sup>3</sup>/y over Europe in 1995-2014.

49 While NO<sub>x</sub> emissions are declining, the shift of NO<sub>x</sub> sources from power generation to  
50 industrial and transportation sectors has led to diminishing effects on NO<sub>x</sub> emission controls  
51 (Jiang et al., 2022). Furthermore, recent studies have demonstrated a slowdown in tropospheric  
52 NO<sub>2</sub> column declines with respect to surface NO<sub>2</sub> concentrations over the US since  
53 approximately 2010 (Jiang et al., 2018; Laughner and Cohen, 2019; Qu et al., 2021). Jiang et  
54 al. (2022) further indicated a slowdown of declines in tropospheric NO<sub>2</sub> columns with respect  
55 to surface NO<sub>2</sub> concentrations over both the US and Europe. Unlike surface O<sub>3</sub>, which is  
56 strongly affected by local emissions, free tropospheric O<sub>3</sub> is more susceptible to the influences

57 of free tropospheric sources and sinks, long-range transport, and stratospheric intrusion (Jiang  
58 et al., 2015; Xue et al., 2021; Trickl et al., 2020). The different trends in surface and free  
59 tropospheric NO<sub>2</sub> may thus result in different changes in surface and free tropospheric O<sub>3</sub> over  
60 the US and Europe.

61 A single O<sub>3</sub> tracer mode (tagged-O<sub>3</sub>) of the GEOS-Chem model was developed in the  
62 companion paper (Zhu et al., 2023) and was combined with Ozone Monitoring Instrument  
63 (OMI) and surface O<sub>3</sub> observations in China in 2015-2020 via a sequential Kalman filter (KF)  
64 assimilation system (Tang et al., 2022; Han et al., 2022). The rapid O<sub>3</sub> assimilation capability  
65 with approximately 91-94% reductions in computational costs (Zhu et al., 2023) provides a  
66 new opportunity to extend atmospheric O<sub>3</sub> observations and mitigate the influence of  
67 uncertainties in physical and chemical processes (Li et al., 2019; Chen et al., 2022) and  
68 emission inventories (Zheng et al., 2017; Jiang et al., 2022). As the second part of this work,  
69 we assimilate OMI and US Air Quality System (AQS) and European AirBase network O<sub>3</sub>  
70 observations in this work to constrain tropospheric O<sub>3</sub> in the US and Europe in 2005-2020 with  
71 a 0.5°×0.625° horizontal resolution. A comparative analysis by assimilating satellite and  
72 surface O<sub>3</sub> observations is useful for better characterization of O<sub>3</sub> changes in the surface and  
73 free troposphere. Furthermore, this analysis helps evaluate the long-term performance of the  
74 GEOS-Chem model in simulating tropospheric O<sub>3</sub> and can provide new insights into  
75 tropospheric O<sub>3</sub> changes accompanied by the reported changes in tropospheric NO<sub>2</sub>.

76 This paper is organized as follows: in Section 2, we provide descriptions for the AQS,  
77 AirBase and OMI O<sub>3</sub> observations and the single O<sub>3</sub> tracer simulation and assimilation system  
78 used in this work. We refer the reader to the companion paper (Zhu et al., 2023) for more details  
79 about the atmospheric O<sub>3</sub> observations and the development and performance of the single O<sub>3</sub>  
80 tracer assimilation system. Tropospheric O<sub>3</sub> changes in the US and Europe in 2005-2020 are  
81 demonstrated in Section 3 by assimilating atmospheric O<sub>3</sub> observations. As shown in Fig. 1,

82 five regions (i.e., Great Lakes (#1), Northeast US (#2), West Coast (#3), Middle US (#4) and  
83 Southeast US (#5)) are defined within the US domain, and five regions (i.e., Britain (#1),  
84 Central EU (#2), Western EU (#3), Iberian Peninsula (#4) and Apennine Peninsula (#5)) are  
85 defined within the European domain based on anthropogenic NO<sub>x</sub> emissions in 2015. Regions  
86 #1-3 (US) and regions #1-2 (Europe) are defined as highly polluted regions by excluding grids  
87 with low and medium anthropogenic NO<sub>x</sub> emissions. Tropospheric O<sub>3</sub> changes over these  
88 regions will be discussed to investigate the possible regional discrepancies in surface and free  
89 tropospheric O<sub>3</sub> changes associated with different local pollution levels. Our conclusions  
90 follow in Section 4.

91

## 92 **2. Data and Methods**

### 93 **2.1 OMI and surface O<sub>3</sub> measurements**

94 The OMI O<sub>3</sub> profile retrieval product (PROFOZ v0.9.3, level 2, Liu et al., 2010; Huang  
95 et al., 2017) from the Smithsonian Astrophysical Observatory (SAO) was assimilated in this  
96 work. The OMI instrument provides global covered measurements with backscattered sunlight  
97 in the ultraviolet–visible range from 270 to 500 nm (UV1: 270–310 nm; UV2: 310–365 nm;  
98 visible: 350–500 nm) with a spatial resolution of 13 × 24 km (nadir view). Following Huang et  
99 al. (2017), the following filters are applied: 1) nearly clear-sky scenes with effective cloud  
100 fraction < 0.3; 2) solar zenith angles (SZA) < 75°; and 3) fitting root mean square (RMS, ratio  
101 of fitting residuals to assumed measurement error) < 2.0. Starting in 2009, anomalies were  
102 found in OMI data and diagnosed as attenuated measured radiances in certain cross-track  
103 positions. This instrument degradation has been referred to as the “row anomaly”. To enhance  
104 the quality and stability of data, only across-track positions between 4-11 (within 30 positions  
105 in the UV1 channels) are used in our analysis. This treatment is similar to the production of  
106 row-isolated data by using across-track positions between 3-18 (within 60 positions in the UV2

107 channels) in the OMI/MLS O<sub>3</sub> data (Ziemke et al., 2019; Wang et al., 2022).

108 We use in situ hourly surface O<sub>3</sub> measurements from the US AQS and European  
109 Environment Agency AirBase networks. The AQS and AirBase networks collect ambient air  
110 pollution data from monitoring stations located in urban, suburban, and rural areas. To ensure  
111 the long-term stability of the observation record, we only considered stations with at least 14  
112 years of observation records in 2005-2020. Observations provided by the AQS and AirBase  
113 stations have been widely used in previous studies to investigate the sources and variabilities  
114 of surface O<sub>3</sub> pollution (Shen et al., 2015; Boleti et al., 2020; He et al., 2022).

## 115 **2.2 Single O<sub>3</sub> tracer simulation and assimilation system**

116 The GEOS-Chem chemical transport model (<http://www.geos-chem.org>, version 12-8-1)  
117 is driven by assimilated meteorological data of MERRA-2. The GEOS-Chem full chemistry  
118 simulation includes fully coupled O<sub>3</sub>-NO<sub>x</sub>-VOC-halogen-aerosol chemistry. Our analysis is  
119 conducted at a horizontal resolution of nested 0.5°×0.625° over the US and Europe with  
120 chemical boundary conditions archived every 3 hours from global simulations with 4°×5°  
121 resolution. Emissions are computed by the Harvard-NASA Emission Component (HEMCO).  
122 Global default anthropogenic emissions are from the CEDS (Community Emissions Data  
123 System) (Hoesly et al., 2018). Regional emissions are replaced by MEIC (Multiresolution  
124 Emission Inventory for China) in China, MIX in other regions of Asia (Li et al., 2017) and  
125 NEI2011 in the US. Open fire emissions are from the Global Fire Emissions Database (GFED4)  
126 (van der Werf et al., 2010).

127 Following Jiang et al. (2022), the total anthropogenic NO<sub>x</sub> and VOC emissions in the  
128 GEOS-Chem model are scaled with the corresponding bottom-up inventories (MEIC for China,  
129 NEI2014 for the US and ECLIPSE for Europe) so that the modeled surface nitrogen dioxide  
130 (NO<sub>2</sub>) and VOC concentrations in the a priori simulations are identical to Jiang et al. (2022) in  
131 2005-2018. The total anthropogenic NO<sub>x</sub> and VOC emissions in 2019-2020 in China, the US

132 and Europe are further scaled based on linear projections. The total anthropogenic NO<sub>x</sub>  
133 emissions in the a priori simulations declined by 53% (US) and 50% (Europe) in 2005-2020.  
134 The total anthropogenic VOC emissions in the a priori simulations declined by 19% (US) and  
135 33% (Europe) in 2005-2020. We refer the reader to Jiang et al. (2022) for the details of the  
136 model configuration and performance, particularly the modeled trends of surface and  
137 tropospheric column NO<sub>2</sub> in 2005-2018.

138 A new single O<sub>3</sub> tracer mode (tagged-O<sub>3</sub>) was developed in the companion paper (Zhu et  
139 al., 2023) by reading the archived production (PO<sub>3</sub>) and loss (LO<sub>3</sub>) of O<sub>3</sub> provided by the full  
140 chemistry simulation. The major advantage of the single O<sub>3</sub> tracer mode is dramatic reductions  
141 in computational costs by approximately 91-94% (Zhu et al., 2023). Fig. S1 and Fig. S2 (see  
142 the SI) show the annual and seasonal averages of surface maximum daily 8-  
143 hour average (MDA8) O<sub>3</sub> over the US and Europe in 2005-2020 from the full chemistry and  
144 single O<sub>3</sub> tracer simulations (i.e., the a priori simulations in this work), respectively. We find  
145 good spatial (Fig. S1 and Fig. S2) as well as temporal (Fig. S3, see the SI) consistencies in  
146 surface MDA8 O<sub>3</sub> between full chemistry and single O<sub>3</sub> tracer simulations over the US and  
147 Europe in 2005-2020. The computation costs (hours of wall time for one year simulation) are  
148 160.7 and 9.4 hours within the nested US domain (0.5°×0.625°) and 103.4 and 6 hours within  
149 the nested Europe domain (0.5°×0.625°) by full chemistry and single O<sub>3</sub> tracer mode,  
150 respectively.

151 The low computational costs of the single O<sub>3</sub> tracer mode allow us to perform O<sub>3</sub>  
152 assimilations more efficiently. The sequential KF was conducted to assimilate AQS, AirBase  
153 and OMI O<sub>3</sub> observations to produce the a posteriori O<sub>3</sub> concentrations. As a brief description  
154 of the assimilation algorithm, the forward model (**M**) predicts the O<sub>3</sub> concentration (**x**<sub>at</sub>) at  
155 time t:

$$156 \quad \mathbf{x}_{at} = \mathbf{M}_t \mathbf{x}_{t-1} \quad (\text{Eq. 1})$$

157 The optimized O<sub>3</sub> concentrations can be expressed as:

$$158 \quad \mathbf{x}_t = \mathbf{x}_{at} + \mathbf{G}_t(\mathbf{y}_t - \mathbf{K}_t\mathbf{x}_{at}) \quad (\text{Eq. 2})$$

159 where  $\mathbf{y}_t$  is the observation (i.e., OMI or surface O<sub>3</sub> observations) and  $\mathbf{K}_t$  represents the  
160 operation operator that projects O<sub>3</sub> concentrations from the model space to the observation  
161 space.  $\mathbf{G}_t$  is the KF gain matrix, which can be described as:

$$162 \quad \mathbf{G}_t = \mathbf{S}_{at}\mathbf{K}_t^T(\mathbf{K}_t\mathbf{S}_{at}\mathbf{K}_t^T + \mathbf{S}_\epsilon)^{-1} \quad (\text{Eq. 3})$$

163 where  $\mathbf{S}_{at}$  and  $\mathbf{S}_\epsilon$  are the model and observation covariances, respectively. The modeled  
164 tropospheric O<sub>3</sub> profiles in the OMI-based assimilation processes are convolved by using the  
165 OMI retrieval averaging kernels. The mixing of O<sub>3</sub> precursors in the planetary boundary layer  
166 is considered with a simplified planetary boundary layer parameterization in surface  
167 observation-based assimilations. We refer the reader to the companion paper (Zhu et al., 2023)  
168 for more details about the development and performance of the single O<sub>3</sub> tracer assimilation  
169 system by assimilating satellite and surface O<sub>3</sub> observations.

170

### 171 **3. Results and Discussion**

#### 172 **3.1 Surface O<sub>3</sub> by assimilating surface O<sub>3</sub> observations**

173 Fig. 2a-e and Fig. 3a-e show the annual and seasonal averages of surface MDA8 O<sub>3</sub>  
174 observations from US AQS and European AirBase stations in 2005-2020. Fig. 2k-o and Fig.  
175 3k-o further show the annual and seasonal averages of the a posteriori O<sub>3</sub> concentrations by  
176 assimilating AQS or AirBase O<sub>3</sub> observations. As shown in Fig. 4 and Fig. 5, the assimilated  
177 O<sub>3</sub> concentrations (blue lines) show good agreements with surface O<sub>3</sub> observations (red lines):  
178 the mean surface MDA8 O<sub>3</sub> in 2005-2020 are 41.4, 39.5 and 39.5 ppb (US), 40.0, 37.7 and  
179 38.2 ppb (Great Lakes), 38.1, 36.4 and 37.4 ppb (Northeast US), 41.6, 41.2 and 41.0 ppb (West  
180 Coast), 42.2, 40.4 and 39.7 ppb (Middle US), 44.4, 40.3 and 39.9 ppb (Southeast US) in the a  
181 priori simulations, a posteriori simulations and AQS observations, respectively; the mean

182 surface MDA8 O<sub>3</sub> in 2005-2020 are 35.3, 32.0 and 31.6 ppb (Europe), 29.9, 26.0 and 24.4 ppb  
183 (Britain), 30.5, 28.2 and 28.0 ppb (Central EU), 35.9, 32.5 and 32.3 ppb (Western EU), 40.3,  
184 35.2 and 34.2 ppb (Iberian Peninsula), 41.8, 35.3 and 34.0 ppb (Apennine Peninsula) in the a  
185 priori simulations, a posteriori simulations and AirBase observations, respectively.

186         Similar to China, we find overestimated summertime surface O<sub>3</sub> concentrations in the a  
187 priori simulations over the US and Europe (Fig. 4 and Fig. 5). However, in contrast to the  
188 underestimated O<sub>3</sub> declines in June-July in China (Zhu et al., 2023), the overestimated  
189 summertime O<sub>3</sub> over the US and Europe are caused by overestimated increases in surface O<sub>3</sub>  
190 in July-August, which have led to surface MDA8 O<sub>3</sub> maximum in July-August in the  
191 simulations. In contrast, assimilations suggest that surface O<sub>3</sub> is broadly maximum in April  
192 over the US and Europe (Fig. 4 and Fig. 5), although O<sub>3</sub> seasonality varies over different  
193 regions. We find good agreements in surface O<sub>3</sub> concentrations between a priori and a  
194 posteriori simulations over the US in seasons outside of summer (Fig. 2p-t), in contrast to the  
195 large differences between a priori and a posteriori simulations over Europe (Fig. 3p-t in this  
196 work) and China (Zhu et al., 2023). The inaccurate surface O<sub>3</sub> concentrations over three  
197 continents reveal possible uncertainties in model simulations, particularly the contributions  
198 from natural and anthropogenic processes; for example, the higher temperature and solar  
199 radiation can lead to high O<sub>3</sub> concentrations in August, whereas the transport of O<sub>3</sub> and its  
200 precursors can lead to high O<sub>3</sub> concentrations in April (Parrish et al., 2013).

201         Furthermore, our analysis exhibits high surface MDA8 O<sub>3</sub> concentrations over the West  
202 Coast (41.2 ppb) in the US. Except for the West Coast, the assimilated surface MDA8 O<sub>3</sub>  
203 concentrations are lower over areas with higher anthropogenic NO<sub>x</sub> emissions over the US and  
204 Europe. For example, 37.7 and 36.4 ppb in the Great Lakes and Northeast US, respectively, in  
205 contrast to 40.4 and 40.3 ppb in the Middle US and Southeast US, respectively; and 26.0 and  
206 28.2 ppb in the Britain and Central EU, respectively, in contrast to 32.5, 35.2 and 35.3 ppb in



207 the Western EU, Iberian Peninsula and Apennine Peninsula, respectively. The inverse  
208 relationships between surface O<sub>3</sub> concentrations and local anthropogenic NO<sub>x</sub> emissions  
209 indicate the important impacts of natural sources and meteorological conditions on surface O<sub>3</sub>  
210 pollution over the US and Europe because of continuous declines in anthropogenic emissions  
211 in the past decades. This is the opposite of the higher O<sub>3</sub> concentrations in areas with higher  
212 local anthropogenic NO<sub>x</sub> emissions in China (Zhu et al., 2023), where surface O<sub>3</sub> pollution is  
213 strongly affected by anthropogenic emissions.

### 214 **3.2 Limited changes in surface O<sub>3</sub> concentrations**

215 Following Jiang et al. (2022), the anthropogenic NO<sub>x</sub> and VOC emissions over the US  
216 in 2005-2020 declined by 53% (-5.1% yr<sup>-1</sup>) and 19% (-1.4% yr<sup>-1</sup>) in our a priori simulations,  
217 which is accompanied by slight decreasing trends in surface MDA8 O<sub>3</sub> in the a priori  
218 simulations (Table 1.1): -0.29 (spring), -0.45 (summer), -0.07 (autumn) and 0.05 (winter) ppb  
219 yr<sup>-1</sup>; and the relative trends are -0.7 (spring), -0.9 (summer), -0.2 (autumn) and 0.2 (winter) %  
220 yr<sup>-1</sup>. Similarly, the anthropogenic NO<sub>x</sub> and VOC emissions over Europe in 2005-2020 declined  
221 by 50% (-4.4% yr<sup>-1</sup>) and 33% (-2.7% yr<sup>-1</sup>) in our a priori simulations, which is accompanied  
222 by slightly increasing trends of surface MDA8 O<sub>3</sub> in the a priori simulations (Table 2.1): -0.07  
223 (spring), -0.07 (summer), 0.07 (autumn) and 0.24 (winter) ppb yr<sup>-1</sup>; and the relative trends are  
224 -0.2 (spring), -0.2 (summer), 0.2 (autumn) and 1.0 (winter) % yr<sup>-1</sup>. It is surprising to see the  
225 limited changes in surface O<sub>3</sub> concentrations in the simulations accompanied by dramatic  
226 declines in anthropogenic emissions.

227 We thus further investigate the changes in surface O<sub>3</sub> by assimilating surface O<sub>3</sub>  
228 observations. As shown in Table 1.1 and Fig. 6k-o, our assimilations suggest -0.27 (spring), -  
229 0.46 (summer), -0.12 (autumn) and 0.11 (winter) ppb yr<sup>-1</sup> changes in surface MDA8 O<sub>3</sub> over  
230 the US in 2005-2020, and the relative changes are -0.6 (spring), -1.0 (summer), -0.3 (autumn)  
231 and 0.4 (winter) % yr<sup>-1</sup>. Similarly, as shown in Table 2.1 and Fig. 7k-o, our assimilations

232 suggest  $-0.04$  (spring),  $-0.03$  (summer),  $0.09$  (autumn) and  $0.19$  (winter)  $\text{ppb yr}^{-1}$  changes in  
233 surface MDA8  $\text{O}_3$  over Europe in 2005-2020, and the relative changes are  $-0.1$  (spring),  $-0.1$   
234 (summer),  $0.3$  (autumn) and  $0.9$  (winter)  $\% \text{ yr}^{-1}$ . In contrast to the underestimated increasing  
235 trends in surface  $\text{O}_3$  concentrations in the a priori simulations in China (Zhu et al., 2023), we  
236 find broadly consistent trends between simulations and assimilations over the US and Europe,  
237 which confirms the limited changes in surface  $\text{O}_3$  concentrations over the US and Europe.

238 The changes in surface  $\text{O}_3$  concentrations have marked regional and seasonal  
239 discrepancies. As shown in Tables S1-S5 (see the SI), our assimilations demonstrate stronger  
240 increasing trends in surface  $\text{O}_3$  concentrations in 2005-2020 in the winter ( $0.39 \text{ ppb yr}^{-1}$  or  $1.5\%$   
241  $\text{yr}^{-1}$ ) over the Great Lakes, in the winter ( $0.36 \text{ ppb yr}^{-1}$  or  $1.4\% \text{ yr}^{-1}$ ) over the Northeast US, in  
242 the autumn ( $0.34 \text{ ppb yr}^{-1}$  or  $0.8\% \text{ yr}^{-1}$ ) and winter ( $0.29 \text{ ppb yr}^{-1}$  or  $1.0\% \text{ yr}^{-1}$ ) over the West  
243 Coast, as well as decreasing trends in surface  $\text{O}_3$  concentrations in 2005-2020 in the summer  
244 over the Great Lakes ( $-0.51 \text{ ppb yr}^{-1}$  or  $-1.0\% \text{ yr}^{-1}$ ), Northeast US ( $-0.52 \text{ ppb yr}^{-1}$  or  $-1.1\% \text{ yr}^{-1}$ ),  
245 Middle US ( $-0.61 \text{ ppb yr}^{-1}$  or  $-1.3\% \text{ yr}^{-1}$ ) and Southeast US ( $-0.87 \text{ ppb yr}^{-1}$  or  $-1.9\% \text{ yr}^{-1}$ ). The  
246 areas with higher anthropogenic  $\text{NO}_x$  emissions such as the Great Lakes and Northeast US  
247 demonstrate lower surface  $\text{O}_3$  concentrations and are accompanied by stronger increasing  
248 trends in the winter and weaker decreasing trends in the summer.

249 Tables S6-S10 (see the SI) further show the details of tropospheric  $\text{O}_3$  changes in Europe.  
250 Our assimilations demonstrate stronger increasing trends in surface  $\text{O}_3$  concentrations in 2005-  
251 2020 in the winter over Britain ( $0.28 \text{ ppb yr}^{-1}$  or  $1.5\% \text{ yr}^{-1}$ ), Central EU ( $0.26 \text{ ppb yr}^{-1}$  or  $1.5\%$   
252  $\text{yr}^{-1}$ ), Western EU ( $0.25 \text{ ppb yr}^{-1}$  or  $1.1\% \text{ yr}^{-1}$ ), Iberian Peninsula ( $0.17 \text{ ppb yr}^{-1}$  or  $0.6\% \text{ yr}^{-1}$ )  
253 and Apennine Peninsula ( $0.18 \text{ ppb yr}^{-1}$  or  $0.8\% \text{ yr}^{-1}$ ), as well as decreasing trends in surface  $\text{O}_3$   
254 concentrations in 2005-2020 in the summer ( $-0.07 \text{ ppb yr}^{-1}$  or  $-0.2\% \text{ yr}^{-1}$ ) over Britain, in the  
255 summer ( $-0.10 \text{ ppb yr}^{-1}$  or  $-0.2\% \text{ yr}^{-1}$ ) over the Western EU, in the summer ( $-0.20 \text{ ppb yr}^{-1}$  or  $-$   
256  $0.5\% \text{ yr}^{-1}$ ) over the Iberian Peninsula and in the spring ( $-0.09 \text{ ppb yr}^{-1}$  or  $-0.2\% \text{ yr}^{-1}$ ) over the

257 Apennine Peninsula. Similar to the US, areas with higher anthropogenic NO<sub>x</sub> emissions such  
258 as Britain and Central EU demonstrate lower surface O<sub>3</sub> concentrations and are accompanied  
259 by stronger increasing trends in the winter and weaker decreasing trends in the summer.

260 Furthermore, Zhu et al. (2023) demonstrated a large discrepancy in the trends in  
261 assimilated surface O<sub>3</sub> between urban (i.e., areas with air quality stations) and regional  
262 backgrounds in China in 2015-2020: 3.0% yr<sup>-1</sup> (sampled at air quality stations) and 1.3% yr<sup>-1</sup>  
263 (land average). In contrast, we did not find a comparable discrepancy over the US and Europe:  
264 the trends of assimilated surface O<sub>3</sub> are -0.4% yr<sup>-1</sup> (Table 1.1, sampled at AQS O<sub>3</sub> observations)  
265 and -0.4% yr<sup>-1</sup> (Table 1.2, land average) over the US and -0.2% yr<sup>-1</sup> (Table 2.1, sampled at  
266 AirBase O<sub>3</sub> observations) and 0.0% yr<sup>-1</sup> (Table 2.2, land average) over Europe. The difference  
267 between China and the US/Europe suggests more consistent changes in surface O<sub>3</sub> between  
268 urban and regional background areas in the US and Europe. This implies possible larger relative  
269 contributions of regional background O<sub>3</sub> to surface O<sub>3</sub> observations in the US and Europe,  
270 which could be associated with the limited changes in surface O<sub>3</sub> concentrations in 2005-2020  
271 because regional background O<sub>3</sub> is less sensitive to changes in anthropogenic NO<sub>x</sub> and VOC  
272 emissions.

### 273 **3.3 Tropospheric O<sub>3</sub> columns by assimilating OMI O<sub>3</sub> observations**

274 Fig. S4a-e and Fig. S5a-e (see the SI) show the annual and seasonal averages of  
275 tropospheric OMI O<sub>3</sub> columns in 2005-2020 over the US and Europe, respectively. Fig. S4k-o  
276 and Fig. S5k-o further show the annual and seasonal averages of the a posteriori tropospheric  
277 O<sub>3</sub> columns by assimilating OMI O<sub>3</sub> observations. The assimilated tropospheric O<sub>3</sub> columns  
278 show good agreement with OMI O<sub>3</sub> observations: the mean tropospheric O<sub>3</sub> columns over the  
279 US in 2005-2020 (Table 1.3) are 35.5 DU in the a priori simulations, and 37.0 and 36.8 DU in  
280 the a posteriori simulations and OMI observations, respectively; the mean tropospheric O<sub>3</sub>  
281 columns over Europe in 2005-2020 (Table 2.3) are 32.8 DU in the a priori simulations, and

282 35.3 and 36.4 DU in the a posteriori simulations and OMI observations, respectively. However,  
283 there are small deviations in the trends between assimilations and OMI observations. As shown  
284 in Fig. S6-S7 (see the SI), the trends of tropospheric O<sub>3</sub> columns over the US in 2005-2020  
285 (Table 1.3) are -0.11 DU yr<sup>-1</sup> in the a priori simulations, and -0.16 and -0.01 DU yr<sup>-1</sup> in the a  
286 posteriori simulations and OMI observations, respectively; the trends of tropospheric O<sub>3</sub>  
287 columns over Europe in 2005-2020 (Table 2.3) are -0.09 DU yr<sup>-1</sup> in the a priori simulations,  
288 and -0.25 and -0.15 DU yr<sup>-1</sup> in the a posteriori simulations and OMI observations, respectively.  
289 These deviations are associated with the adjustments to regional O<sub>3</sub> boundary conditions in the  
290 nested assimilations by assimilating global OMI O<sub>3</sub> observations, reflecting the different  
291 changes in OMI O<sub>3</sub> between US/Europe continents and global backgrounds. For example, the  
292 mean tropospheric O<sub>3</sub> columns over the US in 2005 are 36.5 DU in OMI observations, and 35.9  
293 and 37.5 DU in the assimilations by reading a priori and adjusted O<sub>3</sub> boundary conditions,  
294 respectively; the mean tropospheric O<sub>3</sub> columns over Europe in 2005 are 37.5 DU in OMI  
295 observations, and 34.6 and 36.9 DU in the assimilations by reading a priori and adjusted O<sub>3</sub>  
296 boundary conditions, respectively.

297 The annual averages of surface MDA8 O<sub>3</sub> in the a priori simulation and assimilations are  
298 35.3 and 32.0 ppb with a relative difference of 10% over Europe (Table 2.1); 41.4 and 39.5 ppb  
299 with a relative difference of 5% over the US (Table 1.1); and 42.9 and 41.8 ppb with a relative  
300 difference of 3% over China (Zhu et al., 2023). In addition, the annual averages of tropospheric  
301 O<sub>3</sub> columns in the a priori simulation and assimilations are 32.8 and 35.3 DU with a relative  
302 difference of -7% over Europe (Table 2.3); 35.5 and 37.0 DU with a relative difference of -4%  
303 over the US (Table 1.3); and 37.1 and 37.9 DU with a relative difference of -2% over China  
304 (Zhu et al., 2023). It seems that the GEOS-Chem model has a better performance in regional  
305 averages of surface and free tropospheric O<sub>3</sub> concentrations in China and the US than in  
306 Europe.

307 The output O<sub>3</sub> profiles from a priori and a posteriori simulations are convolved with OMI  
308 averaging kernels in Fig. S4-S7. However, the convolution of OMI O<sub>3</sub> averaging kernels on  
309 the output O<sub>3</sub> profiles can affect the weights of the derived tropospheric columns to O<sub>3</sub> at  
310 different vertical levels and thus may not accurately represent the actual tropospheric O<sub>3</sub>  
311 columns. Fig. 8 and Fig. 9 further show tropospheric O<sub>3</sub> columns from a priori and a posteriori  
312 simulations, in which the output O<sub>3</sub> profiles are not convolved with OMI averaging kernels.  
313 The assimilated tropospheric O<sub>3</sub> columns are 35.6 and 38.7 DU (US), 36.8 and 40.2 DU (Great  
314 Lakes), 36.8 and 40.3 DU (Northeast US), 38.1 and 41.9 DU (West Coast), 38.9 and 41.5 DU  
315 (Middle US), 43.5 and 45.8 DU (Southeast US) in 2005-2020 by assimilating AQS and OMI  
316 O<sub>3</sub> observations, respectively; the assimilated tropospheric O<sub>3</sub> columns are 31.5 and 35.9 DU  
317 (Europe), 29.7 and 34.7 DU (Britain), 30.4 and 34.9 DU (Central EU), 31.8 and 36.4 DU  
318 (Western EU), 33.6 and 38.1 DU (Iberian Peninsula), 34.0 and 38.2 DU (Apennine Peninsula)  
319 in 2005-2020 by assimilating AirBase and OMI O<sub>3</sub> observations, respectively. We find that  
320 tropospheric O<sub>3</sub> columns obtained by assimilating surface O<sub>3</sub> observations are lower than those  
321 obtained by assimilating OMI O<sub>3</sub> observations. Similar to surface O<sub>3</sub> concentrations,  
322 tropospheric O<sub>3</sub> columns are lower over areas with higher anthropogenic NO<sub>x</sub> emissions over  
323 the US and Europe such as the Great Lakes, Northeast US, Britain and Central EU. This is  
324 opposite to the higher tropospheric O<sub>3</sub> columns over areas with higher local anthropogenic NO<sub>x</sub>  
325 emissions in China (Zhu et al., 2023).

326 In contrast to the surface MDA8 O<sub>3</sub> maximum in April in the observations (Fig. 4 and  
327 Fig. 5), the assimilated tropospheric O<sub>3</sub> columns are broadly maximum in July-August over the  
328 US and Europe (Fig. 10 and Fig. 11). The free tropospheric O<sub>3</sub> maximum in the summer has  
329 been reported in previous studies. For example, Wespes et al. (2018) demonstrated a free  
330 tropospheric O<sub>3</sub> maximum in summer over Europe by using Infrared Atmospheric Sounding  
331 Interferometer (IASI) observations; Petetin et al. (2016) exhibited a free tropospheric O<sub>3</sub>

332 maximum in summer over Europe by using MOZAIC aircraft measurements. We find good  
333 agreement in the seasonality of free tropospheric O<sub>3</sub> between simulations and assimilations in  
334 contrast to the inaccurate simulation of the seasonality of surface O<sub>3</sub> concentrations in the  
335 simulations. More studies are needed in the future to explore the sources of this difference in  
336 model performance.

337 Furthermore, Fig. S8-S9 (see the SI) demonstrate the O<sub>3</sub> vertical profiles in 2005-2009,  
338 2010-2014 and 2015-2020, respectively. The assimilation of surface O<sub>3</sub> observations leads to  
339 decreases in O<sub>3</sub> concentrations in the lower troposphere but has small impacts on free  
340 tropospheric O<sub>3</sub>. In contrast, the assimilation of OMI O<sub>3</sub> observations leads to dramatic  
341 enhancements in O<sub>3</sub> concentrations in the middle and upper troposphere without noticeable  
342 differences between areas with high and low local anthropogenic NO<sub>x</sub> emissions. The  
343 enhancement in free tropospheric O<sub>3</sub> by assimilating OMI O<sub>3</sub> observations declined gradually  
344 from 2005-2009 to 2015-2020. The adjustment in free tropospheric O<sub>3</sub> by assimilating OMI O<sub>3</sub>  
345 observations in 2015-2020 is larger but comparable with the adjustment in 2015-2020 in China  
346 (Zhu et al., 2023).

### 347 **3.4 Large decreases in tropospheric O<sub>3</sub> columns**

348 Fig 12 and Fig. 13 show the trends in tropospheric O<sub>3</sub> columns in 2005-2020 from a priori  
349 simulations and a posteriori simulations by assimilating surface and OMI O<sub>3</sub> observations. The  
350 trends of tropospheric O<sub>3</sub> columns in 2005-2020 are -0.07, -0.07 and -0.29 DU yr<sup>-1</sup> (US), -0.03,  
351 -0.03 and -0.29 DU yr<sup>-1</sup> (Great Lakes), -0.02, -0.02 and -0.31 DU yr<sup>-1</sup> (Northeast US), -0.02, -  
352 0.01 and -0.26 DU yr<sup>-1</sup> (West Coast), -0.08, -0.07 and -0.24 DU yr<sup>-1</sup> (Middle US), -0.19, -0.18  
353 and -0.28 DU yr<sup>-1</sup> (Southeast US) in the a priori simulations and a posteriori simulations by  
354 assimilating AQS and OMI O<sub>3</sub> observations, respectively; and are 0.03, 0.03 and -0.36 DU yr<sup>-1</sup>  
355 <sup>1</sup> (Europe), 0.00, 0.00 and -0.49 DU yr<sup>-1</sup> (Britain), 0.04, 0.04 and -0.38 DU yr<sup>-1</sup> (Central EU),  
356 0.02, 0.03 and -0.36 DU yr<sup>-1</sup> (Western EU), 0.02, 0.02 and -0.30 DU yr<sup>-1</sup> (Iberian Peninsula), -

357 0.04, 0.04 and -0.26 DU yr<sup>-1</sup> (Apennine Peninsula) in the a priori simulations and a posteriori  
358 simulations by assimilating AirBase and OMI O<sub>3</sub> observations, respectively. Our analysis thus  
359 exhibits dramatically lower decreasing trends in tropospheric O<sub>3</sub> columns in the a priori  
360 simulations and assimilations by assimilating surface O<sub>3</sub> observations with respect to OMI-  
361 based assimilations.

362 The limited changes in surface O<sub>3</sub> concentrations in the a priori simulations and  
363 assimilations by assimilating surface O<sub>3</sub> observations indicate limited influences of declines in  
364 local anthropogenic emissions on surface O<sub>3</sub> concentrations in the US and Europe in 2005-  
365 2020. We can thus expect insignificant influences of the vertical transport of surface O<sub>3</sub> on the  
366 changes in free tropospheric O<sub>3</sub> over the US and Europe in 2005-2020, as illustrated by the flat  
367 trends in tropospheric O<sub>3</sub> columns in the a priori simulations and assimilations by assimilating  
368 surface O<sub>3</sub> observations (Fig. 10 and Fig. 11), as well as the small impacts of assimilation of  
369 surface O<sub>3</sub> observations on free tropospheric O<sub>3</sub> (Fig. S8-S9). However, as indicated by Jiang  
370 et al. (2022), tropospheric OMI NO<sub>2</sub> columns declined by 36% and 23% in 2005-2018 over the  
371 US and Europe, respectively. Are the large decreases in tropospheric O<sub>3</sub> columns by  
372 assimilating OMI O<sub>3</sub> observations, i.e., 12.0% (US) and 15.0% (Europe) in 2005-2020, caused  
373 by the declines in free tropospheric NO<sub>2</sub>?

374 As indicated by Jiang et al. (2022), tropospheric OMI NO<sub>2</sub> columns declined by -7.0%  
375 yr<sup>-1</sup> (US) and -4.2% yr<sup>-1</sup> (Europe) in 2005-2010, which was followed by a dramatic slowdown  
376 in the decreasing trends, i.e., -1.7% yr<sup>-1</sup> (US) and -1.2% yr<sup>-1</sup> (Europe) in 2010-2018. However,  
377 as shown in Table 1.4, tropospheric O<sub>3</sub> columns obtained by assimilating OMI O<sub>3</sub> observations  
378 declined by -0.3, -2.3 and -0.5% yr<sup>-1</sup> over the US in 2005-2009, 2010-2014 and 2015-2020,  
379 respectively. Similarly, tropospheric O<sub>3</sub> columns obtained by assimilating OMI O<sub>3</sub>  
380 observations declined by -1.0, -2.3 and -0.8% yr<sup>-1</sup> over Europe (Table 2.4) in 2005-2009, 2010-  
381 2014 and 2015-2020, respectively. The OMI-based declines in tropospheric O<sub>3</sub> columns over

382 the US and Europe mainly occurred in the period with slowed decreases in free tropospheric  
383 NO<sub>2</sub> after 2010; in contrast, the dramatic declines in tropospheric NO<sub>2</sub> columns before 2010  
384 were accompanied by limited changes in free tropospheric O<sub>3</sub>. It is thus difficult to conclude  
385 that the large decreases in tropospheric O<sub>3</sub> columns over the US and Europe in 2010-2014 are  
386 dominated by declines in local anthropogenic NO<sub>x</sub> emissions.

387 We note our OMI-based analysis could be affected by the row anomaly issue, although  
388 the usage of “row-isolated” data by using across-track positions between 4-11 in this work is  
389 expected to reduce the impacts of row anomaly. As shown by Huang et al. (2017), the row  
390 anomaly can lead to discontinuity in the trends in OMI O<sub>3</sub> observations in 2009. However, the  
391 large decreases in tropospheric O<sub>3</sub> columns over the US and Europe mainly occurred after  
392 2010. Consequently, we assume a limited influence of row anomaly on our conclusion.  
393 Furthermore, OMI is sensitive to O<sub>3</sub> concentrations in the free troposphere; OMI-based  
394 assimilations are driven by adjusted regional O<sub>3</sub> boundary conditions provided by global OMI  
395 O<sub>3</sub> assimilations and can reflect optimized adjustments in both local and global background O<sub>3</sub>  
396 concentrations. In contrast, surface observations are sensitive to local O<sub>3</sub> concentrations;  
397 surface observation-based assimilations are driven by the a priori O<sub>3</sub> boundary conditions,  
398 which thus reflects the optimized adjustments in local contributions and is also affected by  
399 lacking optimization on the impacts of O<sub>3</sub> precursors due to the single O<sub>3</sub> tracer simulations.  
400 These factors contributed to the difference in the trends of tropospheric O<sub>3</sub> columns by  
401 assimilating surface and satellite observations. Assimilations of both surface and satellite  
402 observations, as shown in this work, are expected to provide more information to better  
403 characterization of the changes and uncertainties in free tropospheric O<sub>3</sub>.

#### 404 **4. Conclusion**

405 As a companion paper of Zhu et al. (2023) which focuses on tropospheric O<sub>3</sub> change in  
406 China in 2015-2020, this paper investigates the changes in surface and free tropospheric O<sub>3</sub>



407 over the US and Europe in 2005-2020 by assimilating OMI, AQS and AirBase O<sub>3</sub> observations.  
408 The assimilated O<sub>3</sub> concentrations demonstrate good agreement with O<sub>3</sub> observations: surface  
409 O<sub>3</sub> concentrations are 41.4, 39.5 and 39.5 ppb (US) and 35.3, 32.0 and 31.6 ppb (Europe) in  
410 the a priori and a posteriori simulations and AQS and AirBase O<sub>3</sub> observations, respectively;  
411 and tropospheric O<sub>3</sub> columns are 35.5, 37.0 and 36.8 DU (US) and 32.8, 35.3 and 36.4 DU  
412 (Europe) in the a priori and a posteriori simulations (convolved with OMI retrieval averaging  
413 kernels) and OMI O<sub>3</sub> observations, respectively. The modeled surface O<sub>3</sub> by GEOS-Chem is  
414 overestimated in the summer, which results in a surface O<sub>3</sub> maximum in July-August in the  
415 simulations in contrast to April in the observations; in contrast, GEOS-Chem demonstrates  
416 good performance in the simulation of seasonality in free tropospheric O<sub>3</sub>, which is maximum  
417 in July-August. In addition, we find lower surface O<sub>3</sub> concentrations over areas with higher  
418 anthropogenic NO<sub>x</sub> emissions in the US and Europe. This is the opposite of the higher O<sub>3</sub>  
419 concentrations in areas with higher local anthropogenic NO<sub>x</sub> emissions in China (Zhu et al.,  
420 2023).

421 Our analysis exhibits a noticeable decrease in surface O<sub>3</sub> concentrations over the US in  
422 the summer by 15% in 2005-2020. However, accompanied by approximately 50% reductions  
423 in NO<sub>x</sub> emissions, changes in surface O<sub>3</sub> concentrations are limited in Europe and other seasons  
424 in the US: the annual surface MDA8 O<sub>3</sub> decreased by -6% over the US and increased by 1.5%  
425 over Europe in 2005-2020, and the decreases in surface O<sub>3</sub> concentrations are weaker over  
426 areas with higher local anthropogenic NO<sub>x</sub> emissions. Furthermore, the surface observation-  
427 based assimilations suggest insignificant changes in tropospheric O<sub>3</sub> columns: -3.0% (US) and  
428 1.5% (Europe) in 2005-2020. While the OMI-based assimilations exhibit large decreases in  
429 tropospheric O<sub>3</sub> columns, i.e., -12.0% (US) and -15.0% (Europe) in 2005-2020, the decreases  
430 in tropospheric O<sub>3</sub> columns mainly occurred in 2010-2014, corresponding to reported slowed  
431 declines in free tropospheric NO<sub>2</sub> since 2010 (Jiang et al., 2022). Despite the dramatic declines

432 in tropospheric NO<sub>2</sub>, particularly, declines in tropospheric NO<sub>2</sub> columns in 2005-2010, our  
433 analysis suggests limited impacts of local emission declines on changes in tropospheric O<sub>3</sub> over  
434 the US and Europe because the rapid decline in tropospheric NO<sub>2</sub> columns in 2005-2010  
435 corresponds to relatively flat trends in tropospheric O<sub>3</sub>. More efforts are suggested to evaluate  
436 the contributions of natural sources and transport to tropospheric O<sub>3</sub> changes, which is critical  
437 for making more effective policies to reduce O<sub>3</sub> pollution.

438

439 **Code and data availability:** The AQS and AirBase surface O<sub>3</sub> data can be downloaded from  
440 <https://www.eea.europa.eu/data-and-maps/data/aqereporting-8> and  
441 [https://aqs.epa.gov/aqsweb/airdata/download\\_files.html#Row](https://aqs.epa.gov/aqsweb/airdata/download_files.html#Row). The OMI PROFOZ product  
442 can be acquired at  
443 <https://avdc.gsfc.nasa.gov/pub/data/satellite/Aura/OMI/V03/L2/OMPROFOZ/>. The GEOS-  
444 Chem model (version 12.8.1) can be downloaded from [http://wiki.seas.harvard.edu/geos-](http://wiki.seas.harvard.edu/geos-chem/index.php/GEOS-Chem_12#12.8.1)  
445 [chem/index.php/GEOS-Chem\\_12#12.8.1](http://wiki.seas.harvard.edu/geos-chem/index.php/GEOS-Chem_12#12.8.1). The KPP module for tagged-O<sub>3</sub> simulations can be  
446 downloaded from <https://doi.org/10.5281/zenodo.7545944>.

447

448 **Competing interests:** The contact author has declared that neither they nor their co-authors  
449 have any competing interests.

450

451 **Acknowledgments:** We thank United States Environmental Protection Agency and the  
452 European Environmental Agency for providing the surface O<sub>3</sub> measurements. The numerical  
453 calculations in this paper have been done on the supercomputing system in the Supercomputing  
454 Center of University of Science and Technology of China. This work was supported by the  
455 Hundred Talents Program of Chinese Academy of Science and National Natural Science  
456 Foundation of China (42277082, 41721002).

457 **Table and Figures**

458 **Table 1.** Averages (with units ppb or DU) and trends (with units ppb yr<sup>-1</sup> or DU yr<sup>-1</sup>) of surface  
459 and tropospheric column O<sub>3</sub> concentrations in 2005-2020 over the US from observations (AQS  
460 and OMI) and a priori and a posteriori (KF) simulations. T1.1): the modeled surface O<sub>3</sub> is  
461 sampled at the locations and times of AQS surface O<sub>3</sub> observations; T1.2): the modeled surface  
462 O<sub>3</sub> is averaged over the US (land only); T1.3): the output O<sub>3</sub> profiles from the a priori and a  
463 posteriori simulations are convolved with OMI O<sub>3</sub> averaging kernels; T1.4): the output O<sub>3</sub>  
464 profiles are NOT convolved with OMI O<sub>3</sub> averaging kernels. The uncertainties in the averages  
465 are calculated using the bootstrapping method. The trends and uncertainties in the trends are  
466 calculated using the linear fitting of averages by using the least squares method (see details in  
467 the SI).

468

469 **Table 2.** Averages (with units ppb or DU) and trends (with units ppb yr<sup>-1</sup> or DU yr<sup>-1</sup>) of surface  
470 and tropospheric column O<sub>3</sub> concentrations in 2005-2020 over Europe from observations  
471 (AirBase and OMI) and a priori and a posteriori (KF) simulations. T2.1): the modeled surface  
472 O<sub>3</sub> are sampled at the locations and times of AirBase surface O<sub>3</sub> observations; T2.2): the  
473 modeled surface O<sub>3</sub> are averaged over Europe (land only); T2.3): the output O<sub>3</sub> profiles from  
474 the a priori and a posteriori simulations are convolved with OMI O<sub>3</sub> averaging kernels; T2.4):  
475 the output O<sub>3</sub> profiles are NOT convolved with OMI O<sub>3</sub> averaging kernels.

476

477 **Fig. 1.** (a) Anthropogenic NO<sub>x</sub> emissions over the US in 2015; (b) Region definitions for Great  
478 Lakes (#1), Northeast US (#2), West Coast (#3), Middle US (#4) and Southeast US (#5).  
479 Regions #1-3 are defined as highly polluted (HP) regions by excluding grids with low and  
480 medium anthropogenic NO<sub>x</sub> emissions. (c) Anthropogenic NO<sub>x</sub> emissions over Europe in 2015;  
481 (d) Region definitions for Britain (#1), Central EU (#2), Western EU (#3), Iberian Peninsula  
482 (#4) and Apennine Peninsula (#5). Regions #1 and #2 are defined as highly polluted (HP)  
483 regions by excluding grids with low and medium anthropogenic NO<sub>x</sub> emissions. The different  
484 colors (red, gray and green) represent grids with high (highest 15%), medium (15-50%) and  
485 low (lowest 50%) anthropogenic NO<sub>x</sub> emissions.

486

487 **Fig. 2.** Surface MDA8 O<sub>3</sub> over the US in 2005-2020 (annual and seasonal averages) from (a-  
488 e) AQS stations; (f-j) GEOS-Chem a priori simulation; (k-o) GEOS-Chem a posteriori

489 simulation by assimilating AQS O<sub>3</sub> observations. (p-t) Bias in the a priori simulations  
490 calculated by a priori minus a posteriori O<sub>3</sub> concentrations.

491

492 **Fig. 3.** Surface MDA8 O<sub>3</sub> over Europe in 2005-2020 (annual and seasonal averages) from (a-  
493 e) AirBase stations; (f-j) GEOS-Chem a priori simulation; (k-o) GEOS-Chem a posteriori  
494 simulation by assimilating AirBase O<sub>3</sub> observations. (p-t) Bias in the a priori simulations  
495 calculated by a priori minus a posteriori O<sub>3</sub> concentrations.

496

497 **Fig. 4.** (a-f) Daily averages of surface MDA8 O<sub>3</sub> over the US in 2005-2020 from AQS stations  
498 (red) and GEOS-Chem a priori (black) and a posteriori (blue) simulations by assimilating AQS  
499 O<sub>3</sub> observations. (g-l) Monthly averages of MDA8 O<sub>3</sub>. The dashed lines in panels g-l are annual  
500 averages.

501

502 **Fig. 5.** (a-f) Daily averages of surface MDA8 O<sub>3</sub> over Europe in 2005-2020 from AirBase  
503 stations (red) and GEOS-Chem a priori (black) and a posteriori (blue) simulations by  
504 assimilating AirBase O<sub>3</sub> observations. (g-l) Monthly averages of MDA8 O<sub>3</sub>. The dashed lines  
505 in panels g-l are annual averages.

506

507 **Fig. 6.** Trends of surface MDA8 O<sub>3</sub> over the US in 2005-2020 (annual and seasonal averages)  
508 from (a-e) AQS stations; (f-j) GEOS-Chem a priori simulation; (k-o) GEOS-Chem a posteriori  
509 simulation by assimilating AQS O<sub>3</sub> observations.

510

511 **Fig. 7.** Trends of surface MDA8 O<sub>3</sub> over Europe in 2005-2020 (annual and seasonal averages)  
512 from (a-e) AirBase stations; (f-j) GEOS-Chem a priori simulation; (k-o) GEOS-Chem a  
513 posteriori simulation by assimilating AirBase O<sub>3</sub> observations.

514

515 **Fig. 8.** Tropospheric O<sub>3</sub> columns over the US in 2005-2020 (annual and seasonal averages)  
516 from (a-e) GEOS-Chem a priori simulation; (f-j) Assimilations of AQS surface O<sub>3</sub>  
517 observations; (k-o) Assimilations of OMI O<sub>3</sub> observations. (p-t) Difference in tropospheric O<sub>3</sub>  
518 columns calculated by OMI-based assimilations minus surface observation-based  
519 assimilations.

520

521 **Fig. 9.** Tropospheric O<sub>3</sub> columns over Europe in 2005-2020 (annual and seasonal averages)  
522 from (a-e) GEOS-Chem a priori simulation; (f-j) Assimilations of AirBase surface O<sub>3</sub>

523 observations; (k-o) Assimilations of OMI O<sub>3</sub> observations. (p-t) Difference in tropospheric O<sub>3</sub>  
524 columns calculated by OMI-based assimilations minus surface observation-based  
525 assimilations.

526

527 **Fig. 10.** (a-f) Daily averages of tropospheric O<sub>3</sub> columns over the US in 2005-2020 from  
528 GEOS-Chem a priori simulation (black) and a posteriori simulations by assimilating AQS  
529 (blue) and OMI (red) O<sub>3</sub> observations. (g-l) Monthly averages of tropospheric O<sub>3</sub> columns. The  
530 dashed lines in panels g-l are annual averages.

531

532 **Fig. 11.** (a-f) Daily averages of tropospheric O<sub>3</sub> columns over Europe in 2005-2020 from  
533 GEOS-Chem a priori simulation (black) and a posteriori simulations by assimilating AirBase  
534 (blue) and OMI (red) O<sub>3</sub> observations. (g-l) Monthly averages of tropospheric O<sub>3</sub> columns. The  
535 dashed lines in panels g-l are annual averages.

536

537 **Fig. 12.** Trends of tropospheric O<sub>3</sub> columns over the US in 2005-2020 (annual and seasonal  
538 averages) from (a-e) GEOS-Chem a priori simulation; (f-j) Assimilations of AQS surface O<sub>3</sub>  
539 observations; (k-o) Assimilations of OMI O<sub>3</sub> observations.

540

541 **Fig. 13.** Trends of tropospheric O<sub>3</sub> columns over Europe in 2005-2020 (annual and seasonal  
542 averages) from (a-e) GEOS-Chem a priori simulation; (f-j) Assimilations of AirBase surface  
543 O<sub>3</sub> observations; (k-o) Assimilations of OMI O<sub>3</sub> observations.

544

## 545 **References**

- 546 Boleti, E., Hueglin, C., Grange, S. K., Prévôt, A. S. H., and Takahama, S.: Temporal and spatial  
547 analysis of ozone concentrations in Europe based on timescale decomposition and a multi-  
548 clustering approach, *Atmos Chem Phys*, 20, 9051-9066, 10.5194/acp-20-9051-2020, 2020.
- 549 Chen, J., Jiang, Z., Li, R., Liao, C., Miyazaki, K., and Jones, D. B. A.: Large discrepancy  
550 between observed and modeled wintertime tropospheric NO<sub>2</sub> variabilities due to COVID-19  
551 controls in China, *Environ Res Lett*, 17, 035007, 10.1088/1748-9326/ac4ec0, 2022.
- 552 Chen, X., Jiang, Z., Shen, Y., Li, R., Fu, Y., Liu, J., Han, H., Liao, H., Cheng, X., Jones, D. B.  
553 A., Worden, H., and Abad, G. G.: Chinese Regulations Are Working—Why Is Surface Ozone  
554 Over Industrialized Areas Still High? Applying Lessons From Northeast US Air Quality  
555 Evolution, *Geophys Res Lett*, 48, e2021GL092816, 10.1029/2021gl092816, 2021.
- 556 Crippa, M., Janssens-Maenhout, G., Dentener, F., Guizzardi, D., Sindelarova, K., Muntean,  
557 M., Van Dingenen, R., and Granier, C.: Forty years of improvements in European air quality:

558 regional policy-industry interactions with global impacts, *Atmos Chem Phys*, 16, 3825-3841,  
559 10.5194/acp-16-3825-2016, 2016.

560 Di, Q., Amini, H., Shi, L., Kloog, I., Silvern, R., Kelly, J., Sabath, M. B., Choirat, C., Koutrakis,  
561 P., Lyapustin, A., Wang, Y., Mickley, L. J., and Schwartz, J.: Assessing NO<sub>2</sub> Concentration  
562 and Model Uncertainty with High Spatiotemporal Resolution across the Contiguous United  
563 States Using Ensemble Model Averaging, *Environ Sci Technol*, 54, 1372-1384,  
564 10.1021/acs.est.9b03358, 2020.

565 United States Environmental Protection Agency: Overview of the Clean Air Act and Air  
566 Pollution: <https://www.epa.gov/clean-air-act-overview>, 2017.

567 Han, W., He, T.-L., Tang, Z., Wang, M., Jones, D., and Jiang, Z.: A comparative analysis for  
568 a deep learning model (hyDL-CO v1.0) and Kalman filter to predict CO concentrations in  
569 China, *Geosci Model Dev*, 15, 4225-4237, 10.5194/gmd-15-4225-2022, 2022.

570 He, T.-L., Jones, D. B. A., Miyazaki, K., Huang, B., Liu, Y., Jiang, Z., White, E. C., Worden,  
571 H. M., and Worden, J. R.: Deep learning to evaluate US NO<sub>x</sub> emissions using surface ozone  
572 predictions, *J Geophys Res-Atmos*, e2021JD035597, 10.1029/2021jd035597, 2022.

573 Hoesly, R. M., Smith, S. J., Feng, L., Klimont, Z., Janssens-Maenhout, G., Pitkanen, T.,  
574 Seibert, J. J., Vu, L., Andres, R. J., Bolt, R. M., Bond, T. C., Dawidowski, L., Kholod, N.,  
575 Kurokawa, J.-i., Li, M., Liu, L., Lu, Z., Moura, M. C. P., O'Rourke, P. R., and Zhang, Q.:  
576 Historical (1750–2014) anthropogenic emissions of reactive gases and aerosols from the  
577 Community Emissions Data System (CEDS), *Geosci Model Dev*, 11, 369-408, 10.5194/gmd-  
578 11-369-2018, 2018.

579 Huang, G., Liu, X., Chance, K., Yang, K., Bhartia, P. K., Cai, Z., Allaart, M., Ancellet, G.,  
580 Calpini, B., Coetzee, G. J. R., Cuevas-Agulló, E., Cupeiro, M., De Backer, H., Dubey, M. K.,  
581 Fuelberg, H. E., Fujiwara, M., Godin-Beekmann, S., Hall, T. J., Johnson, B., Joseph, E., Kivi,  
582 R., Kois, B., Komala, N., König-Langlo, G., Laneve, G., Leblanc, T., Marchand, M.,  
583 Minschwaner, K. R., Morris, G., Newchurch, M. J., Ogino, S.-Y., Ohkawara, N., Piters, A. J.  
584 M., Posny, F., Querel, R., Scheele, R., Schmidlin, F. J., Schnell, R. C., Schrems, O., Selkirk,  
585 H., Shiotani, M., Skrivánková, P., Stübi, R., Taha, G., Tarasick, D. W., Thompson, A. M.,  
586 Thouret, V., Tully, M. B., Van Malderen, R., Vömel, H., von der Gathen, P., Witte, J. C., and  
587 Yela, M.: Validation of 10-year SAO OMI Ozone Profile (PROFOZ) product using  
588 ozonesonde observations, *Atmos Meas Tech*, 10, 2455-2475, 10.5194/amt-10-2455-2017,  
589 2017.

590 Jiang, Z., Worden, J. R., Jones, D. B. A., Lin, J. T., Verstraeten, W. W., and Henze, D. K.:  
591 Constraints on Asian ozone using Aura TES, OMI and Terra MOPITT, *Atmos Chem Phys*,  
592 15, 99-112, 10.5194/acp-15-99-2015, 2015.

593 Jiang, Z., McDonald, B. C., Worden, H., Worden, J. R., Miyazaki, K., Qu, Z., Henze, D. K.,  
594 Jones, D. B. A., Arellano, A. F., Fischer, E. V., Zhu, L., and Boersma, K. F.: Unexpected  
595 slowdown of US pollutant emission reduction in the past decade, *Proc Natl Acad Sci USA*,  
596 115, 5099-5104, 10.1073/pnas.1801191115, 2018.

597 Jiang, Z., Zhu, R., Miyazaki, K., McDonald, B. C., Klimont, Z., Zheng, B., Boersma, K. F.,  
598 Zhang, Q., Worden, H., Worden, J. R., Henze, D. K., Jones, D. B. A., Denier van der Gon,  
599 H. A. C., and Eskes, H.: Decadal Variabilities in Tropospheric Nitrogen Oxides Over United

600 States, Europe, and China, *J Geophys Res-Atmos*, 127, e2021JD035872,  
601 10.1029/2021jd035872, 2022.

602 Laughner, J. L., and Cohen, R. C.: Direct observation of changing NO<sub>x</sub> lifetime in North  
603 American cities, *Science*, 366, 723-727, 10.1126/science.aax6832, 2019.

604 Li, K., Jacob, D. J., Liao, H., Zhu, J., Shah, V., Shen, L., Bates, K. H., Zhang, Q., and Zhai, S.:  
605 A two-pollutant strategy for improving ozone and particulate air quality in China, *Nat Geosci*,  
606 12, 906-910, 10.1038/s41561-019-0464-x, 2019.

607 Li, M., Zhang, Q., Kurokawa, J.-i., Woo, J.-H., He, K., Lu, Z., Ohara, T., Song, Y., Streets, D.  
608 G., Carmichael, G. R., Cheng, Y., Hong, C., Huo, H., Jiang, X., Kang, S., Liu, F., Su, H., and  
609 Zheng, B.: MIX: a mosaic Asian anthropogenic emission inventory under the international  
610 collaboration framework of the MICS-Asia and HTAP, *Atmos Chem Phys*, 17, 935-963,  
611 10.5194/acp-17-935-2017, 2017.

612 Macdonald, E., Otero, N., and Butler, T.: A comparison of long-term trends in observations  
613 and emission inventories of NO<sub>x</sub>, *Atmos Chem Phys*, 21, 4007-4023, 10.5194/acp-21-4007-  
614 2021, 2021.

615 Parrish, D. D., Law, K. S., Staehelin, J., Derwent, R., Cooper, O. R., Tanimoto, H., Volz-  
616 Thomas, A., Gilge, S., Scheel, H. E., Steinbacher, M., and Chan, E.: Lower tropospheric  
617 ozone at northern midlatitudes: Changing seasonal cycle, *Geophys Res Lett*, 40, 1631-1636,  
618 10.1002/grl.50303, 2013.

619 Petetin, H., Thouret, V., Fontaine, A., Sauvage, B., Athier, G., Blot, R., Boulanger, D., Cousin,  
620 J.-M., and Nédélec, P.: Characterising tropospheric O<sub>3</sub> and CO  
621 around Frankfurt over the period 1994–2012 based on MOZAIC–IAGOS aircraft  
622 measurements, *Atmos Chem Phys*, 16, 15147-15163, 10.5194/acp-16-15147-2016, 2016.

623 Qu, Z., Jacob, D. J., Silvern, R. F., Shah, V., Campbell, P. C., Valin, L. C., and Murray, L. T.:  
624 US COVID - 19 Shutdown Demonstrates Importance of Background NO<sub>2</sub> in Inferring NO<sub>x</sub>  
625 Emissions From Satellite NO<sub>2</sub> Observations, *Geophys Res Lett*, 48, 10.1029/2021gl092783,  
626 2021.

627 Seltzer, K. M., Shindell, D. T., Kasibhatla, P., and Malley, C. S.: Magnitude, trends, and  
628 impacts of ambient long-term ozone exposure in the United States from 2000 to 2015, *Atmos*  
629 *Chem Phys*, 20, 1757-1775, 10.5194/acp-20-1757-2020, 2020.

630 Shen, L., Mickley, L. J., and Tai, A. P. K.: Influence of synoptic patterns on surface ozone  
631 variability over the eastern United States from 1980 to 2012, *Atmos Chem Phys*, 15, 10925-  
632 10938, 10.5194/acp-15-10925-2015, 2015.

633 Tang, Z., Chen, J., and Jiang, Z.: Discrepancy in assimilated atmospheric CO over East Asia  
634 in 2015–2020 by assimilating satellite and surface CO measurements, *Atmos Chem Phys*, 22,  
635 7815-7826, 10.5194/acp-22-7815-2022, 2022.

636 Trickl, T., Vogelmann, H., Ries, L., and Sprenger, M.: Very high stratospheric influence  
637 observed in the free troposphere over the northern Alps – just a local phenomenon?, *Atmos*  
638 *Chem Phys*, 20, 243-266, 10.5194/acp-20-243-2020, 2020.

639 van der Werf, G. R., Randerson, J. T., Giglio, L., Collatz, G. J., Mu, M., Kasibhatla, P. S.,  
640 Morton, D. C., DeFries, R. S., Jin, Y., and van Leeuwen, T. T.: Global fire emissions and the

641 contribution of deforestation, savanna, forest, agricultural, and peat fires (1997–2009), *Atmos*  
642 *Chem Phys*, 10, 11707-11735, 10.5194/acp-10-11707-2010, 2010.

643 Wang, X., Fu, T. M., Zhang, L., Lu, X., Liu, X., Amnuaylojaroen, T., Latif, M. T., Ma, Y.,  
644 Zhang, L., Feng, X., Zhu, L., Shen, H., and Yang, X.: Rapidly Changing Emissions Drove  
645 Substantial Surface and Tropospheric Ozone Increases Over Southeast Asia, *Geophys Res*  
646 *Lett*, 49, e2022GL100223, 10.1029/2022gl100223, 2022.

647 Wespes, C., Hurtmans, D., Clerbaux, C., Boynard, A., and Coheur, P.-F.: Decrease in  
648 tropospheric O<sub>3</sub> levels in the Northern Hemisphere observed by IASI, *Atmos Chem Phys*, 18,  
649 6867-6885, 10.5194/acp-18-6867-2018, 2018.

650 Xue, L., Ding, A., Cooper, O., Huang, X., Wang, W., Zhou, D., Wu, Z., McClure-Begley, A.,  
651 Petropavlovskikh, I., Andreae, M. O., and Fu, C.: ENSO and Southeast Asian biomass  
652 burning modulate subtropical trans-Pacific ozone transport, *Natl Sci Rev*, 8, nwaa132,  
653 10.1093/nsr/nwaa132, 2021.

654 Yan, Y., Pozzer, A., Ojha, N., Lin, J., and Lelieveld, J.: Analysis of European ozone trends in  
655 the period 1995–2014, *Atmos Chem Phys*, 18, 5589-5605, 10.5194/acp-18-5589-2018, 2018.

656 Zheng, B., Zhang, Q., Tong, D., Chen, C., Hong, C., Li, M., Geng, G., Lei, Y., Huo, H., and  
657 He, K.: Resolution dependence of uncertainties in gridded emission inventories: a case study  
658 in Hebei, China, *Atmos Chem Phys*, 17, 921-933, 10.5194/acp-17-921-2017, 2017.

659 Zhu, R., Tang, Z., Chen, X., Liu, X., and Jiang, Z.: Rapid O<sub>3</sub> assimilations – Part 1:  
660 methodology and tropospheric O<sub>3</sub> changes in China in 2015-2020, *Geosci. Model Dev.*  
661 *Discuss.*, in review, 10.5194/gmd-2023-35, 2023.

662 Ziemke, J. R., Oman, L. D., Strode, S. A., Douglass, A. R., Olsen, M. A., McPeters, R. D.,  
663 Bhartia, P. K., Froidevaux, L., Labow, G. J., Witte, J. C., Thompson, A. M., Haffner, D. P.,  
664 Kramarova, N. A., Frith, S. M., Huang, L.-K., Jaross, G. R., Seftor, C. J., Deland, M. T., and  
665 Taylor, S. L.: Trends in global tropospheric ozone inferred from a composite record of  
666 TOMS/OMI/MLS/OMPS satellite measurements and the MERRA-2 GMI simulation, *Atmos*  
667 *Chem Phys*, 19, 3257-3269, 10.5194/acp-19-3257-2019, 2019.

668



United States			Annual		Spring		Summer		Autumn		Winter	
			Mean	Trend	Mean	Trend	Mean	Trend	Mean	Trend	Mean	Trend
T1.1 surface (sampled)	2005- 2020	AQS	39.5±0.2	-0.18±0.04	45.4±0.2	-0.26±0.06	45.2±0.3	-0.49±0.10	36.2±0.2	-0.18±0.09	31.5±0.3	0.14±0.05
		a priori	41.4±0.2	-0.18±0.04	44.2±0.1	-0.29±0.04	51.2±0.3	-0.45±0.11	39.2±0.2	-0.07±0.06	30.9±0.2	0.05±0.05
		KF-AQS	39.5±0.2	-0.17±0.04	44.8±0.1	-0.27±0.05	46.0±0.3	-0.46±0.10	36.3±0.2	-0.12±0.07	31.1±0.2	0.11±0.04
T1.2 surface	2005- 2020	a priori	40.3±0.1	-0.17±0.04	43.3±0.1	-0.28±0.05	49.1±0.1	-0.36±0.10	38.1±0.1	-0.10±0.05	30.8±0.1	0.04±0.05
		KF-AQS	39.2±0.1	-0.15±0.03	43.5±0.1	-0.25±0.04	46.1±0.1	-0.34±0.09	36.4±0.1	-0.12±0.05	31.0±0.1	0.07±0.04
T1.3 trop. column (convolved)	2005- 2020	OMI	36.8±0.1	-0.01±0.05	38.5±0.1	0.00±0.09	42.1±0.1	0.11±0.08	34.3±0.1	-0.14±0.05	32.0±0.1	-0.03±0.10
		a priori	35.5±0.1	-0.11±0.03	36.9±0.1	-0.14±0.07	41.9±0.1	-0.15±0.06	33.5±0.1	-0.08±0.03	29.8±0.1	-0.06±0.04
		KF-OMI	37.0±0.1	-0.16±0.04	39.4±0.1	-0.21±0.07	43.3±0.1	-0.02±0.06	34.6±0.1	-0.18±0.04	30.7±0.1	-0.21±0.04
T1.4 trop. Column	2005- 2020	a priori	35.9±0.1	-0.07±0.04	37.4±0.1	-0.16±0.08	41.2±0.1	-0.17±0.09	33.4±0.1	-0.01±0.06	31.6±0.1	0.02±0.07
		KF-AQS	35.6±0.1	-0.07±0.04	37.4±0.1	-0.15±0.08	40.4±0.1	-0.16±0.09	33.1±0.1	-0.01±0.06	31.6±0.1	0.02±0.07
		KF-OMI	38.7±0.1	-0.29±0.04	41.9±0.1	-0.42±0.09	43.9±0.1	-0.11±0.09	35.6±0.1	-0.26±0.06	33.3±0.1	-0.41±0.10
	2005- 2009	KF-AQS	35.7±0.1	-0.25±0.14	37.7±0.2	-0.45±0.39	40.7±0.1	-0.97±0.21	32.9±0.1	-0.12±0.35	31.5±0.2	-0.13±0.33
		KF-OMI	40.1±0.1	-0.13±0.18	43.5±0.1	-0.21±0.40	43.5±0.1	-0.70±0.13	37.1±0.1	-0.18±0.48	36.5±0.1	-0.35±0.32
	2010- 2014	KF-AQS	36.1±0.1	-0.51±0.26	38.3±0.1	-0.78±0.62	41.3±0.1	-1.31±0.39	33.3±0.1	-0.17±0.31	31.5±0.1	-0.30±0.65
		KF-OMI	39.1±0.1	-0.89±0.14	43.3±0.1	-1.20±0.56	45.1±0.1	-1.37±0.37	35.4±0.1	-0.41±0.31	31.9±0.1	-0.67±0.63
	2015- 2020	KF-AQS	35.1±0.1	0.03±0.11	36.5±0.1	-0.05±0.30	39.6±0.1	0.15±0.35	32.9±0.1	0.04±0.31	31.8±0.1	0.09±0.29
KF-OMI		37.1±0.1	-0.18±0.13	39.5±0.1	-0.43±0.39	43.2±0.1	-0.02±0.28	34.4±0.1	-0.21±0.25	31.8±0.1	-0.03±0.27	

**Table 1.** Averages (with units ppb or DU) and trends (with units ppb yr<sup>-1</sup> or DU yr<sup>-1</sup>) of surface and tropospheric column O<sub>3</sub> concentrations in 2005-2020 over the US from observations (AQS and OMI) and a priori and a posteriori (KF) simulations. T1.1): the modeled surface O<sub>3</sub> is sampled at the locations and times of AQS surface O<sub>3</sub> observations; T1.2): the modeled surface O<sub>3</sub> is averaged over the US (land only); T1.3): the output O<sub>3</sub> profiles from the a priori and a posteriori simulations are convolved with OMI O<sub>3</sub> averaging kernels; T1.4): the output O<sub>3</sub> profiles are NOT convolved with OMI O<sub>3</sub> averaging kernels. The uncertainties in the averages are calculated using the bootstrapping method. The trends and uncertainties in the trends are calculated using the linear fitting of averages by using the least squares method (see details in the SI).

Europe			Annual		Spring		Summer		Autumn		Winter	
			Mean	Trend	Mean	Trend	Mean	Trend	Mean	Trend	Mean	Trend
T2.1 surface (sampled)	2005- 2020	AirBase	31.6±0.2	0.08±0.04	38.5±0.1	-0.02±0.06	40.7±0.2	0.01±0.11	25.7±0.2	0.14±0.05	21.4±0.2	0.22±0.05
		a priori	35.3±0.2	0.04±0.03	40.3±0.2	-0.07±0.04	46.6±0.2	-0.07±0.09	31.5±0.2	0.07±0.05	22.9±0.2	0.24±0.05
		KF-AirBase	32.0±0.1	0.05±0.04	38.5±0.1	-0.04±0.06	41.3±0.2	-0.03±0.10	26.6±0.2	0.09±0.05	21.7±0.1	0.19±0.04
T2.2 surface	2005- 2020	a priori	35.5±0.1	0.01±0.02	40.3±0.1	-0.10±0.04	46.0±0.2	-0.09±0.08	31.8±0.2	0.04±0.04	23.9±0.2	0.21±0.05
		KF-AirBase	32.5±0.1	0.01±0.03	38.5±0.1	-0.08±0.04	41.1±0.2	-0.08±0.09	27.7±0.1	0.04±0.04	22.8±0.1	0.17±0.04
T2.3 trop. column (convolved)	2005- 2020	OMI	36.4±0.1	-0.15±0.06	37.6±0.1	-0.33±0.14	41.0±0.1	-0.09±0.08	34.5±0.1	-0.12±0.07	32.5±0.1	-0.09±0.11
		a priori	32.8±0.1	-0.09±0.03	33.6±0.1	-0.18±0.06	37.3±0.1	-0.14±0.06	31.3±0.1	-0.03±0.02	29.0±0.0	-0.02±0.05
		KF-OMI	35.3±0.1	-0.25±0.04	37.0±0.1	-0.40±0.09	40.5±0.1	-0.16±0.06	33.1±0.1	-0.22±0.04	30.4±0.0	-0.23±0.05
T2.4 trop. Column	2005- 2020	a priori	32.1±0.1	0.03±0.03	33.7±0.1	-0.03±0.06	37.2±0.1	0.06±0.05	29.5±0.1	0.01±0.04	27.9±0.0	0.06±0.05
		KF-AirBase	31.5±0.1	0.03±0.03	33.3±0.1	-0.03±0.06	36.2±0.1	0.06±0.05	28.8±0.1	0.01±0.04	27.7±0.1	0.06±0.05
		KF-OMI	35.9±0.1	-0.36±0.04	39.5±0.1	-0.48±0.07	41.4±0.1	0.02±0.06	32.1±0.1	-0.38±0.05	30.4±0.0	-0.58±0.11
	2005- 2009	KF-AirBase	31.2±0.1	-0.24±0.08	33.1±0.0	-0.17±0.26	35.8±0.1	-0.39±0.12	28.6±0.0	-0.40±0.21	27.3±0.0	-0.22±0.30
		KF-OMI	38.1±0.0	-0.38±0.22	41.6±0.1	-0.35±0.39	40.9±0.1	-0.06±0.23	34.6±0.0	-0.76±0.33	34.9±0.0	-1.06±0.44
	2010- 2014	KF-AirBase	31.4±0.1	-0.24±0.23	33.6±0.0	-0.58±0.46	35.8±0.1	-0.33±0.32	28.7±0.1	-0.02±0.30	27.4±0.0	-0.16±0.34
		KF-OMI	35.7±0.1	-0.82±0.12	40.6±0.1	-1.30±0.25	41.6±0.1	-0.54±0.33	31.5±0.1	-0.40±0.19	28.3±0.0	-0.69±0.27
2015- 2020	KF-AirBase	31.7±0.1	0.03±0.09	33.1±0.1	-0.03±0.20	36.8±0.1	0.00±0.22	28.9±0.1	0.09±0.13	28.2±0.0	-0.02±0.20	
	KF-OMI	34.3±0.1	-0.26±0.11	36.9±0.1	-0.58±0.14	41.6±0.1	-0.28±0.33	30.5±0.1	-0.19±0.15	28.5±0.0	-0.11±0.20	

**Table 2.** Averages (with units ppb or DU) and trends (with units ppb yr<sup>-1</sup> or DU yr<sup>-1</sup>) of surface and tropospheric column O<sub>3</sub> concentrations in 2005-2020 over Europe from observations (AirBase and OMI) and a priori and a posteriori (KF) simulations. T2.1): the modeled surface O<sub>3</sub> are sampled at the locations and times of AirBase surface O<sub>3</sub> observations; T2.2): the modeled surface O<sub>3</sub> are averaged over Europe (land only); T2.3): the output O<sub>3</sub> profiles from the a priori and a posteriori simulations are convolved with OMI O<sub>3</sub> averaging kernels; T2.4): the output O<sub>3</sub> profiles are NOT convolved with OMI O<sub>3</sub> averaging kernels.

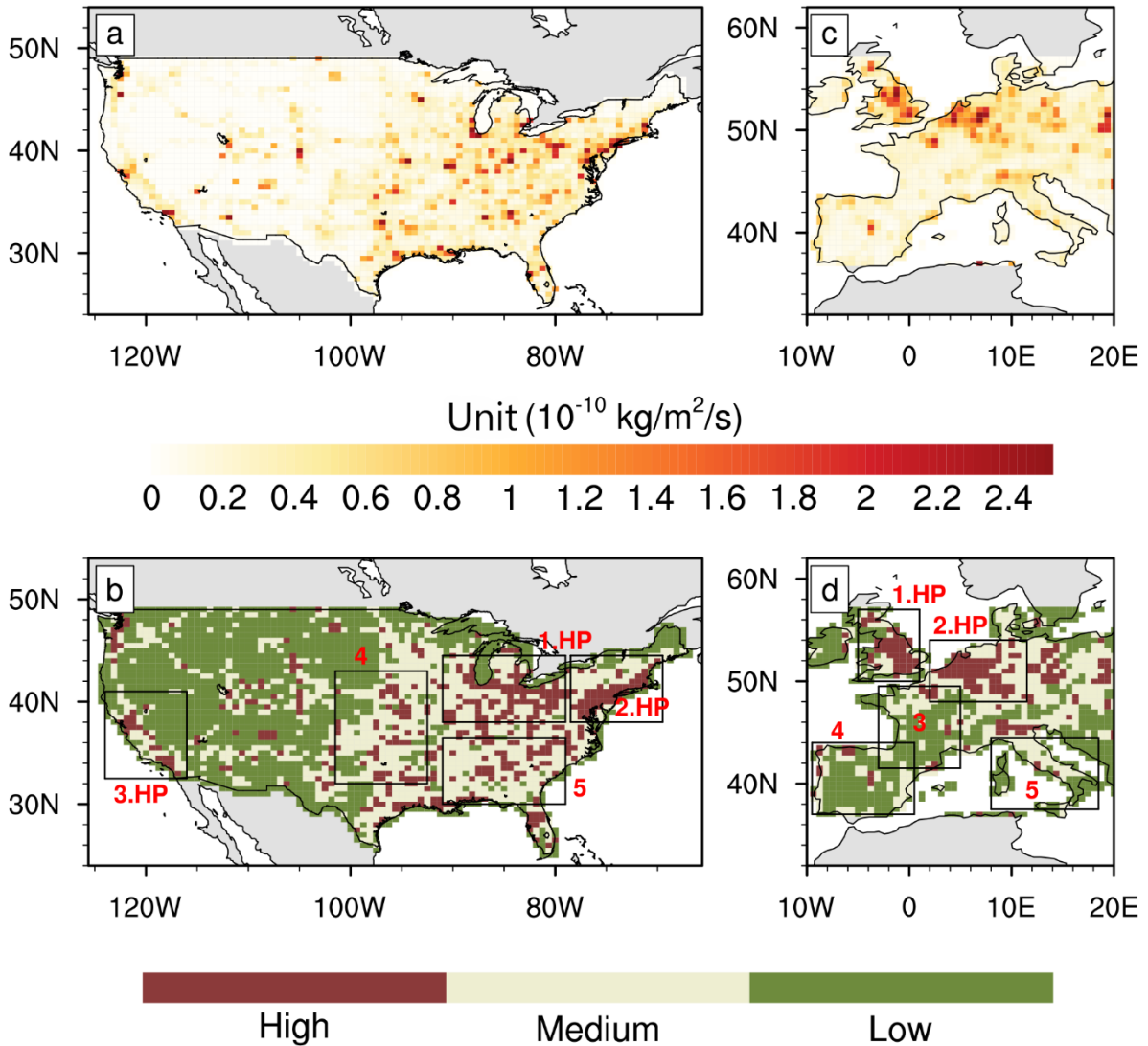


**Fig. 1.** (a) Anthropogenic NO<sub>x</sub> emissions over the US in 2015; (b) Region definitions for Great Lakes (#1), Northeast US (#2), West Coast (#3), Middle US (#4) and Southeast US (#5). Regions #1-3 are defined as highly polluted (HP) regions by excluding grids with low and medium anthropogenic NO<sub>x</sub> emissions. (c) Anthropogenic NO<sub>x</sub> emissions over Europe in 2015; (d) Region definitions for Britain (#1), Central EU (#2), Western EU (#3), Iberian Peninsula (#4) and Apennine Peninsula (#5). Regions #1 and #2 are defined as highly polluted (HP) regions by excluding grids with low and medium anthropogenic NO<sub>x</sub> emissions. The different colors (red, gray and green) represent grids with high (highest 15%), medium (15-50%) and low (lowest 50%) anthropogenic NO<sub>x</sub> emissions.

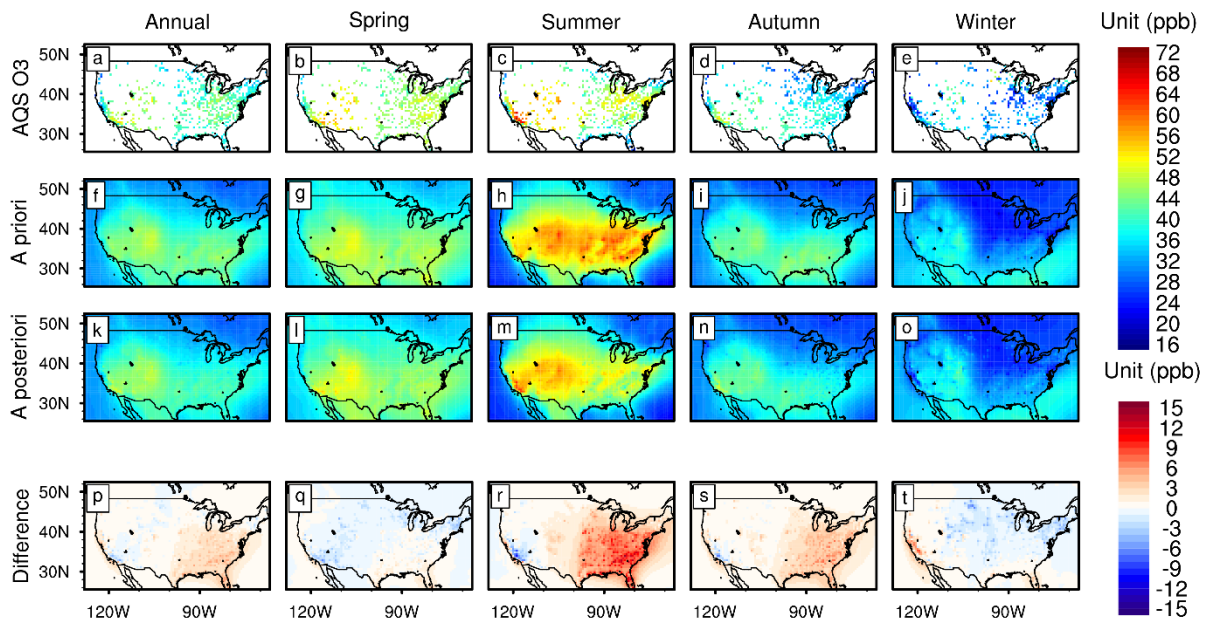


**Fig. 2.** Surface MDA8 O<sub>3</sub> over the US in 2005-2020 (annual and seasonal averages) from (a-e) AQS stations; (f-j) GEOS-Chem a priori simulation; (k-o) GEOS-Chem a posteriori simulation by assimilating AQS O<sub>3</sub> observations. (p-t) Bias in the a priori simulations calculated by a priori minus a posteriori O<sub>3</sub> concentrations.

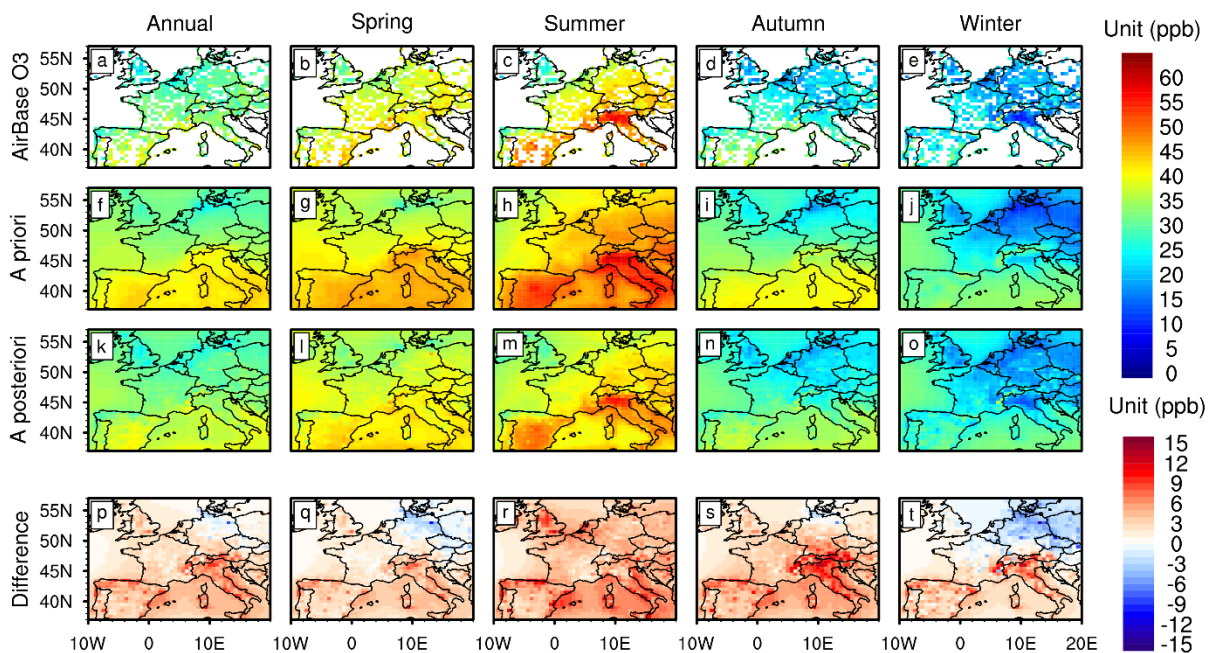


**Fig. 3.** Surface MDA8 O<sub>3</sub> over Europe in 2005-2020 (annual and seasonal averages) from (a-e) AirBase stations; (f-j) GEOS-Chem a priori simulation; (k-o) GEOS-Chem a posteriori simulation by assimilating AirBase O<sub>3</sub> observations. (p-t) Bias in the a priori simulations calculated by a priori minus a posteriori O<sub>3</sub> concentrations.

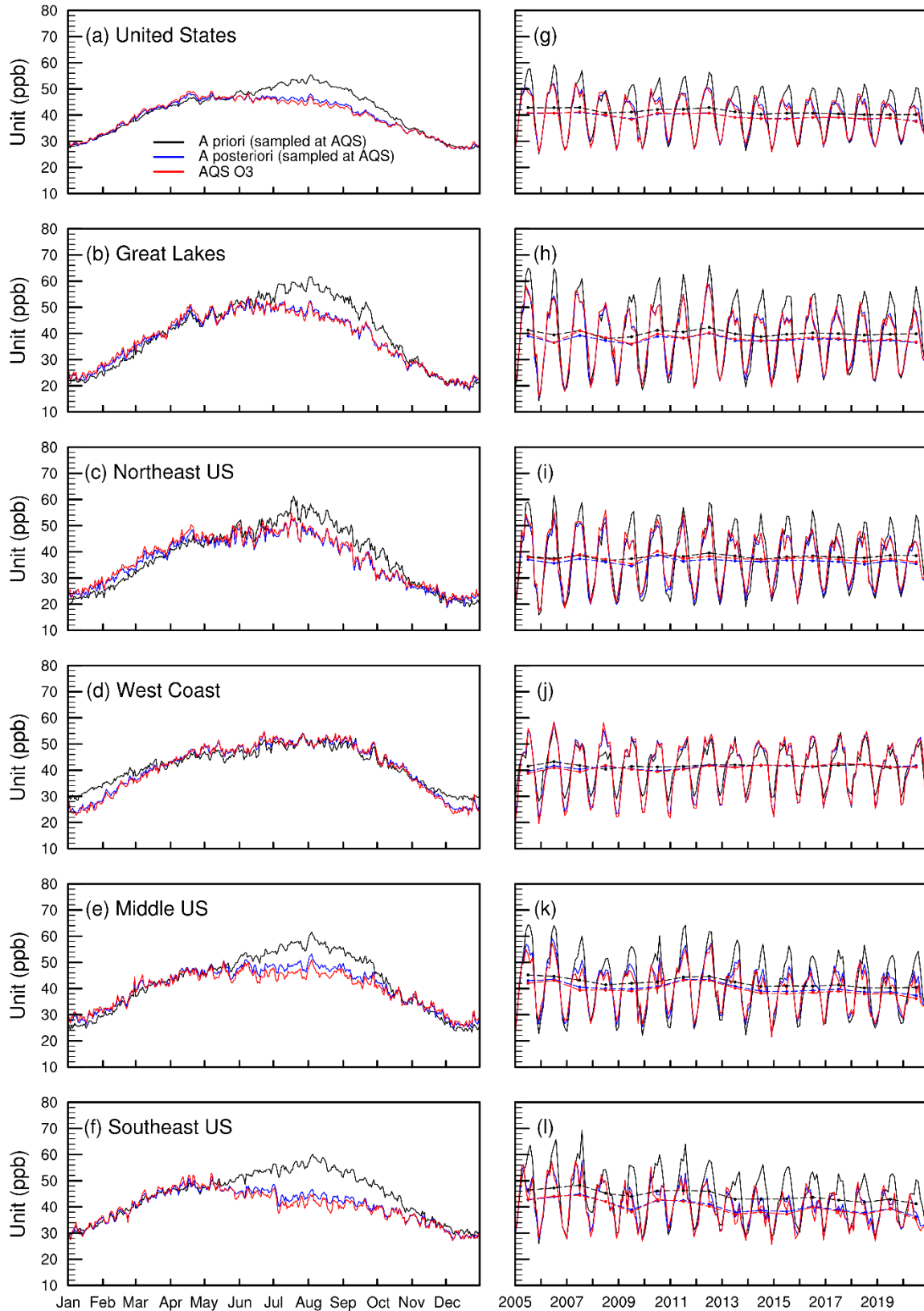


**Fig. 4.** (a-f) Daily averages of surface MDA8 O<sub>3</sub> over the US in 2005-2020 from AQS stations (red) and GEOS-Chem a priori (black) and a posteriori (blue) simulations by assimilating AQS O<sub>3</sub> observations. (g-l) Monthly averages of MDA8 O<sub>3</sub>. The dashed lines in panels g-l are annual averages.

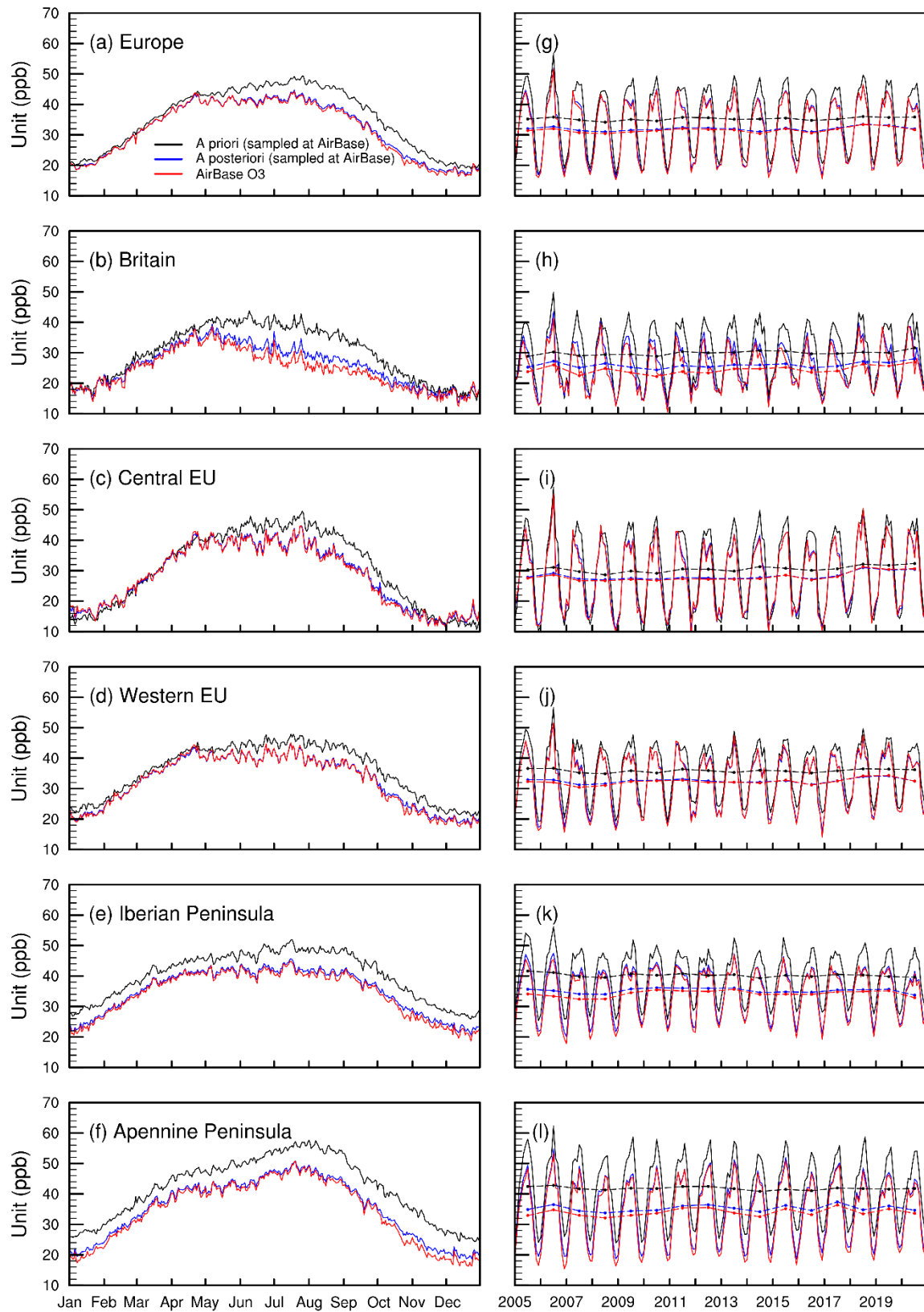


**Fig. 5.** (a-f) Daily averages of surface MDA8 O<sub>3</sub> over Europe in 2005-2020 from AirBase stations (red) and GEOS-Chem a priori (black) and a posteriori (blue) simulations by assimilating AirBase O<sub>3</sub> observations. (g-l) Monthly averages of MDA8 O<sub>3</sub>. The dashed lines in panels g-l are annual averages.

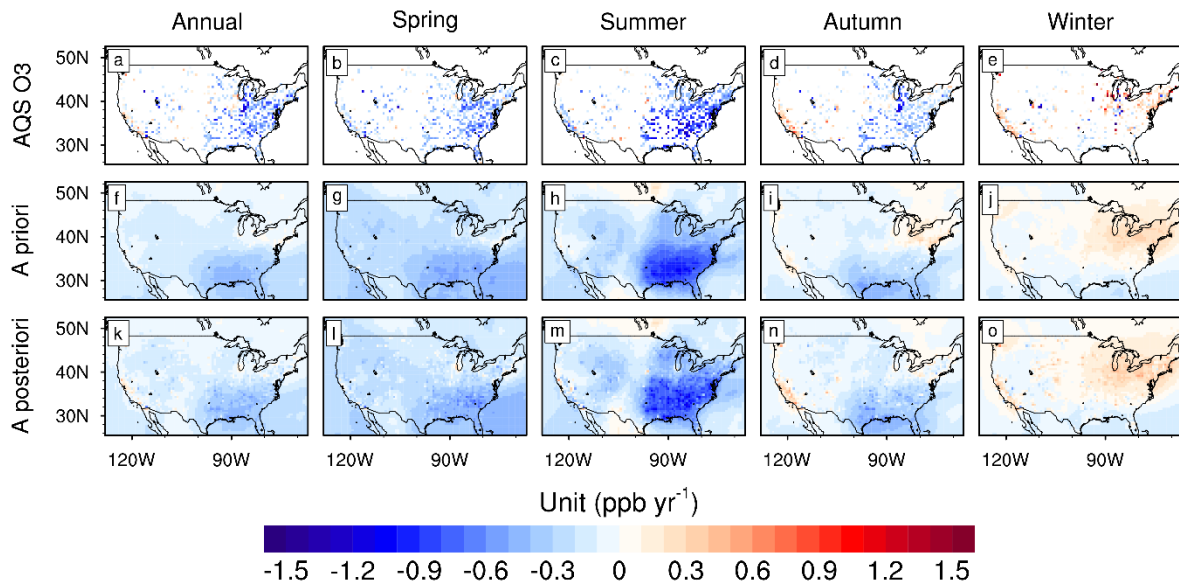


**Fig. 6.** Trends of surface MDA8 O<sub>3</sub> over the US in 2005-2020 (annual and seasonal averages) from (a-e) AQS stations; (f-j) GEOS-Chem a priori simulation; (k-o) GEOS-Chem a posteriori simulation by assimilating AQS O<sub>3</sub> observations.

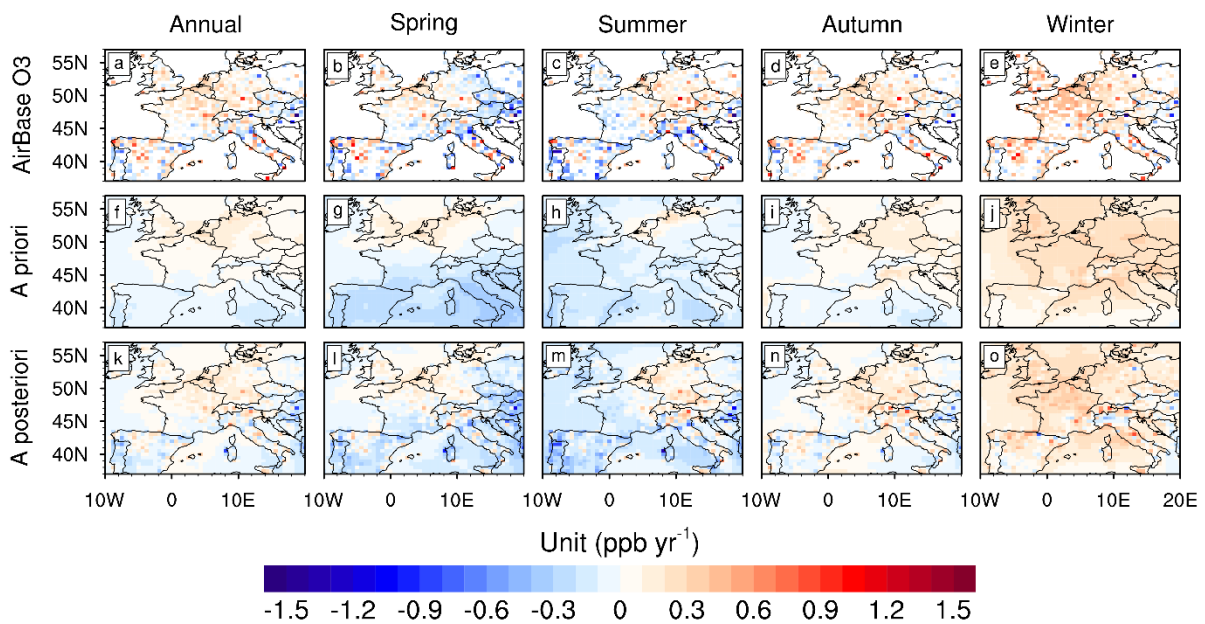


**Fig. 7.** Trends of surface MDA8 O<sub>3</sub> over Europe in 2005-2020 (annual and seasonal averages) from (a-e) AirBase stations; (f-j) GEOS-Chem a priori simulation; (k-o) GEOS-Chem a posteriori simulation by assimilating AirBase O<sub>3</sub> observations.

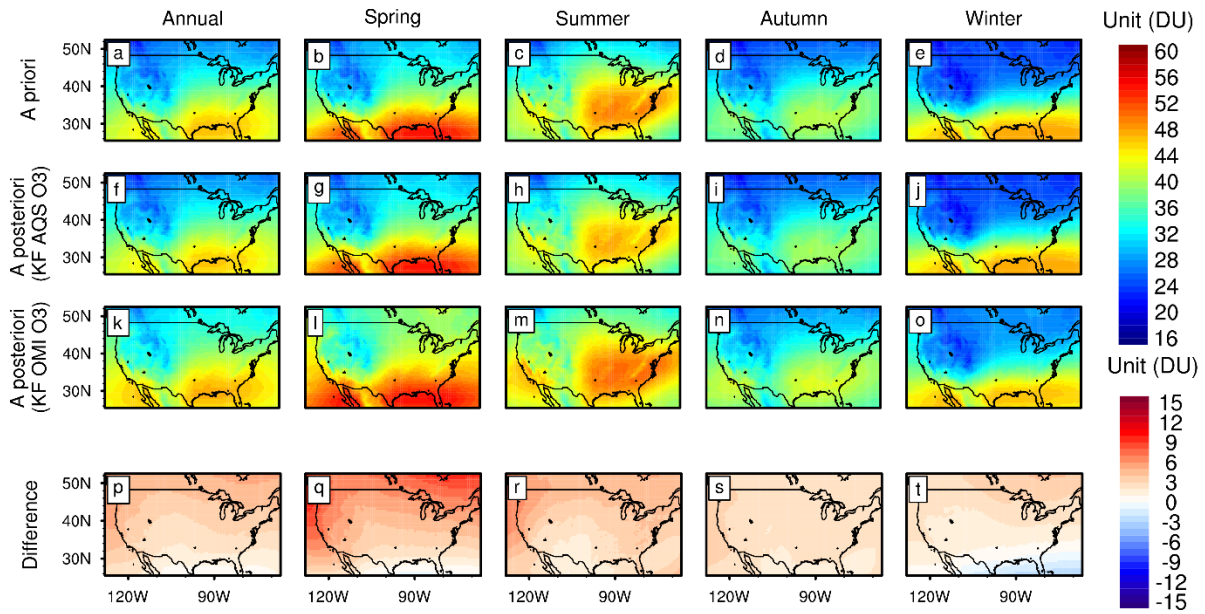


**Fig. 8.** Tropospheric O<sub>3</sub> columns over the US in 2005-2020 (annual and seasonal averages) from (a-e) GEOS-Chem a priori simulation; (f-j) Assimilations of AQS surface O<sub>3</sub> observations; (k-o) Assimilations of OMI O<sub>3</sub> observations. (p-t) Difference in tropospheric O<sub>3</sub> columns calculated by OMI-based assimilations minus surface observation-based assimilations.

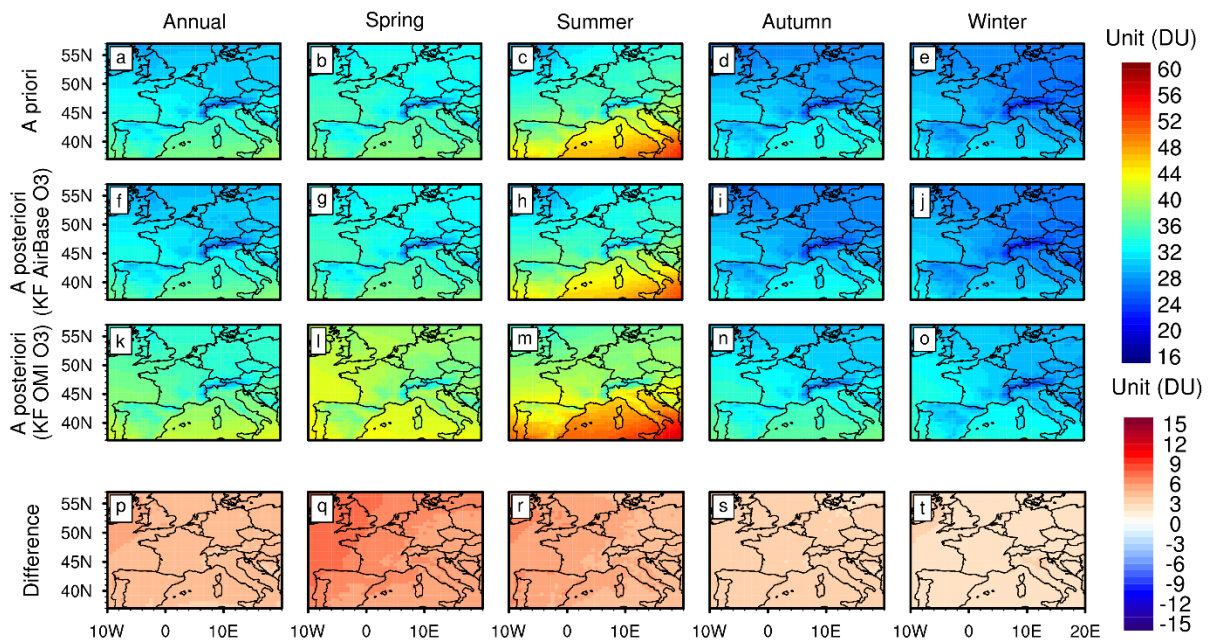


**Fig. 9.** Tropospheric O<sub>3</sub> columns over Europe in 2005-2020 (annual and seasonal averages) from (a-e) GEOS-Chem a priori simulation; (f-j) Assimilations of AirBase surface O<sub>3</sub> observations; (k-o) Assimilations of OMI O<sub>3</sub> observations. (p-t) Difference in tropospheric O<sub>3</sub> columns calculated by OMI-based assimilations minus surface observation-based assimilations.



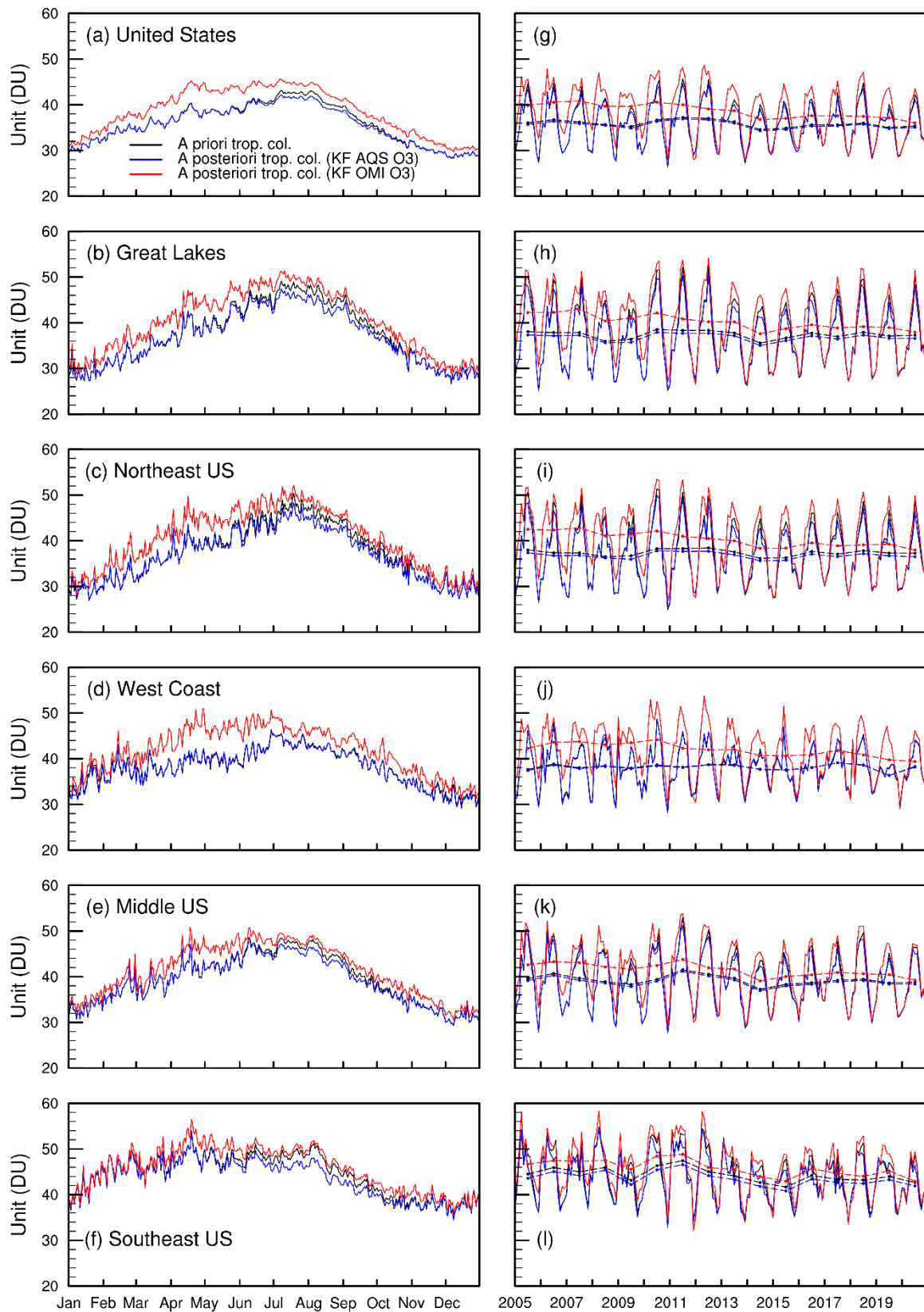


**Fig. 10.** (a-f) Daily averages of tropospheric O<sub>3</sub> columns over the US in 2005-2020 from GEOS-Chem a priori simulation (black) and a posteriori simulations by assimilating AQS (blue) and OMI (red) O<sub>3</sub> observations. (g-l) Monthly averages of tropospheric O<sub>3</sub> columns. The dashed lines in panels g-l are annual averages.

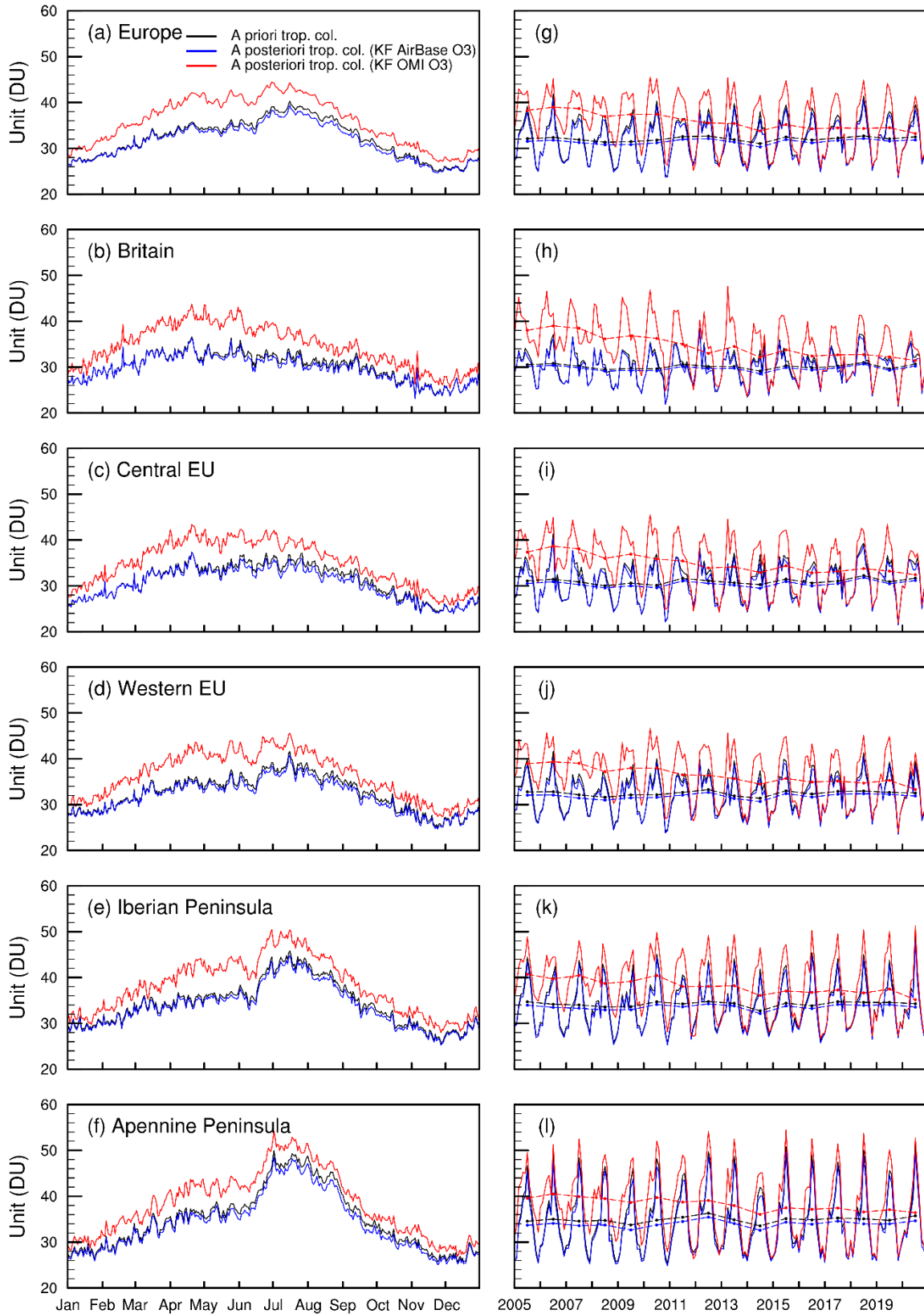


**Fig. 11.** (a-f) Daily averages of tropospheric O<sub>3</sub> columns over Europe in 2005-2020 from GEOS-Chem a priori simulation (black) and a posteriori simulations by assimilating AirBase (blue) and OMI (red) O<sub>3</sub> observations. (g-l) Monthly averages of tropospheric O<sub>3</sub> columns. The dashed lines in panels g-l are annual averages.

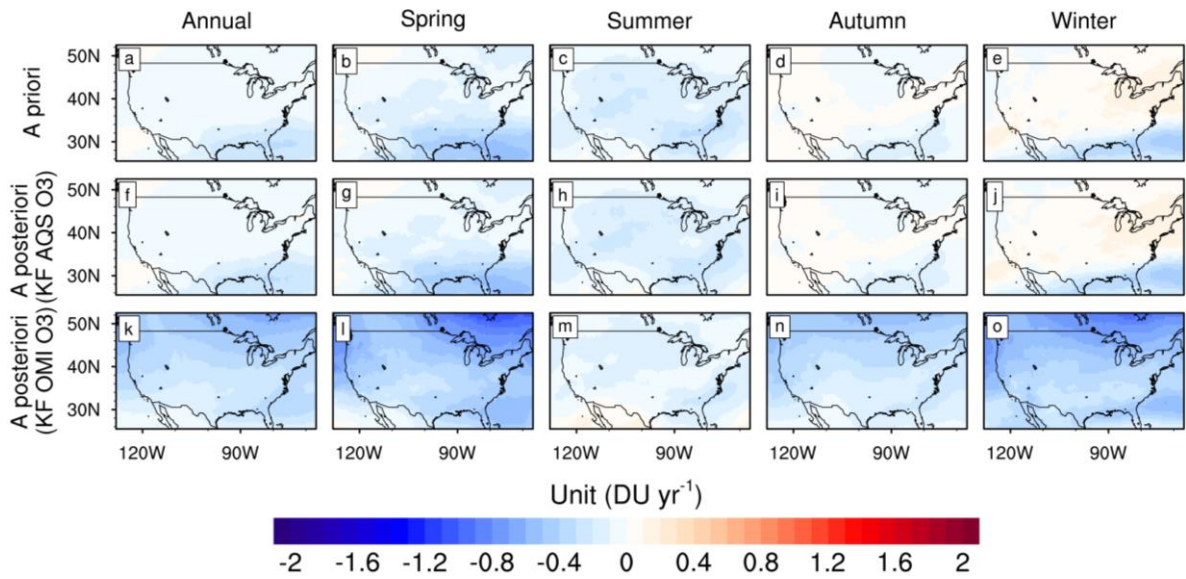


**Fig. 12.** Trends of tropospheric O<sub>3</sub> columns over the US in 2005-2020 (annual and seasonal averages) from (a-e) GEOS-Chem a priori simulation; (f-j) Assimilations of AQS surface O<sub>3</sub> observations; (k-o) Assimilations of OMI O<sub>3</sub> observations.

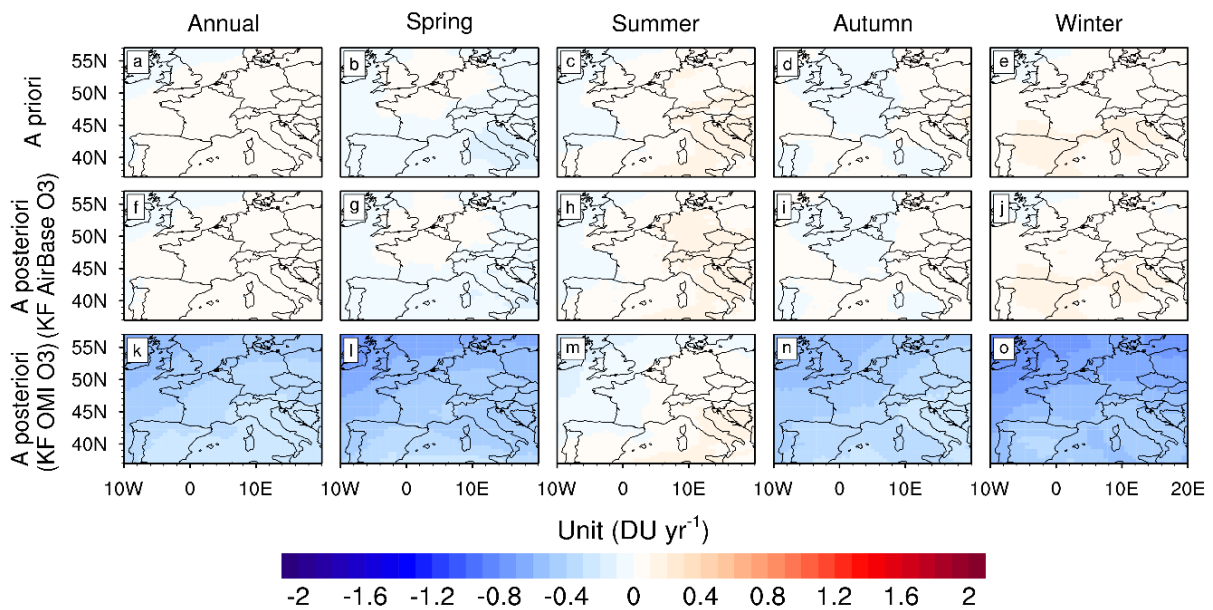


**Fig. 13.** Trends of tropospheric O<sub>3</sub> columns over Europe in 2005-2020 (annual and seasonal averages) from (a-e) GEOS-Chem a priori simulation; (f-j) Assimilations of AirBase surface O<sub>3</sub> observations; (k-o) Assimilations of OMI O<sub>3</sub> observations.